



Hydrodynamic Simulations of Pre-supernova Outbursts in Red Supergiants: Asphericity and Mass Loss

Shing-Chi Leung and Jim Fuller

TAPIR, Walter Burke Institute for Theoretical Physics, Mailcode 350-17, Caltech, Pasadena, CA 91125, USA; shingchi.leung@ipmu.jp

Received 2020 June 25; revised 2020 July 31; accepted 2020 August 3; published 2020 September 7

Abstract

The activity of a massive star approaching core-collapse can strongly affect the appearance of the star and its subsequent supernova. Late-phase convective nuclear burning generates waves that propagate toward the stellar surface, heating the envelope and potentially triggering mass loss. In this work, we improve on previous one-dimensional models by performing two-dimensional simulations of the pre-supernova mass ejection phase due to deposition of wave energy. Beginning with stellar evolutionary models of a $15 M_{\odot}$ red supergiant star during core O-burning, we treat the rate and duration of energy deposition as model parameters and examine the mass-loss dependence and the pre-explosion morphology accordingly. Unlike one-dimensional models, density inversions due to wave heating are smoothed by Rayleigh–Taylor instabilities, and the primary effect of wave heating is to radially expand the star’s hydrogen envelope. For low heating rates with long durations, the expansion is nearly homologous, whereas high but short-lived heating can generate a shock that drives envelope expansion and results in a qualitatively different density profile at the time of core-collapse. Asymmetries are fairly small, and large amounts of mass loss are unlikely unless the wave heating exceeds expectations. We discuss implications for pre-supernova stellar variability and supernovae light curves.

Unified Astronomy Thesaurus concepts: [Stellar evolution \(1599\)](#); [Hydrodynamical simulations \(767\)](#); [Stellar atmospheres \(1584\)](#)

1. Introduction

1.1. Pre-supernova Stellar Evolution

Type II supernovae (SNe) are the explosions of massive hydrogen-rich stars, and it is widely accepted that the progenitors of Type II-P SNe are red supergiants. Observations indicate that progenitor stars of interacting Type IIn SNe usually produce pre-SN outbursts (Ofek et al. 2014), specific examples including SN 2009ip (Mauerhan et al. 2013), SN 2010mc (Ofek et al. 2013), and SN 2015bh (Elias-Rosa et al. 2016; Ofek et al. 2016). However, even fairly typical Type II-P SNe show evidence for circumstellar material (CSM) that may arise from pre-SN mass loss (Khazov et al. 2016; Yaron et al. 2017). Pre-SN mass eruption events have also been observed or hinted at in other types of SNe, including Type IIb such as SN 2013cu (Gal-Yam et al. 2014; Groh 2014; Gräfener & Vink 2016), Type Ibn such as SN 2006jc (Pastorello et al. 2007), SN 2015G (Shivvers et al. 2017), and SN 2015U (Shivvers et al. 2016), and even broad-lined Type Ic such as PTF11qej (Corsi et al. 2014) and SN 2018gep (Ho et al. 2019).

Pre-SN mass ejection has been proposed to explain many features of both ordinary and superluminous SNe. The interaction between the ejecta from the final core-collapse explosion and the previously ejected CSM allows the efficient conversion of the ejecta kinetic energy to thermal energy by shock heating. A classical example is pulsation pair-instability SNe (Woosley et al. 2007; Yoshida et al. 2016; Woosley 2018; Leung et al. 2019a). Shock waves driven by unstable oxygen burning eject large amounts of mass prior to the star’s collapse, creating dense CSM that allows for a superluminous SN (Sorokina et al. 2016; Morozova et al. 2017; Tolstov et al. 2017).

For less massive stars, wave energy transport within the progenitor may be able to trigger smaller amounts of pre-SN

mass loss (see, e.g., Quataert & Shiode 2012). Due to the large rate of energy generation by nuclear reactions, convective motions near the star’s core become very energetic during advanced burning phases such as carbon, neon, oxygen, and silicon burning (e.g., Woosley et al. 2002). The convective motion generates gravity waves that carry a power L_{wave} that scales with the convective luminosity L_{con} as $L_{\text{wave}} \sim M_{\text{con}} L_{\text{con}}$ (Goldreich & Kumar 1990; Alvan et al. 2015), where M_{con} is the mean Mach number of the convective motion. The gravity waves propagate outward and are partially reflected by overlying convective shells, though some wave energy is still transferred outward into acoustic waves after tunneling through these evanescent regions (see, e.g., Fuller et al. 2015; Takata 2016 for applications in low-mass red giant stars).

The acoustic waves dissipate via weak shock formation when the rate of energy transport by waves exceeds the maximum possible wave flux (Ro & Matzner 2017), which drops rapidly at the transition from the helium shell to the hydrogen envelope. The thermalized wave energy, depending on how fast it is injected, can trigger expansion of the envelope and also mass ejection (Fuller 2017). Recent studies of observational data have shown that pre-SN activity may be important for explaining the shape of the light curve (Moriya et al. 2017, 2018; Morozova et al. 2017, 2018), though too much wave heat (or heat deposited over too long a duration) is inconsistent with typical Type II-P SNe (Ouchi & Maeda 2019). Instead, more impulsive wave heating is favored based on light-curve modeling of SN 2017eaw, confirming that such energy deposition can better reproduce SN light curves (Morozova et al. 2020).

We note that wave-driven outbursts may not occur in many SN progenitors, as demonstrated by SN progenitor monitoring (Kochanek et al. 2017; Johnson et al. 2018) that rules out luminous and long-lasting outbursts in several nearby Type II-P

SNe. The purpose of this paper is not to determine the frequency or likelihood of wave-driven outbursts, but rather their effect on the progenitor’s structure if they do occur.

1.2. Motivation

Fuller (2017) and Fuller & Ro (2018) compute one-dimensional stellar evolutionary models for a $15 M_{\odot}$ star model with and without a hydrogen envelope. They demonstrate that wave heat has very different effects in hydrogen-rich and hydrogen-poor stars. In the latter, the energy can eject $\sim 10^{-2}$ – $10^{-1} M_{\odot}$ in an optically thick super-Eddington wind from the surface of the star. In hydrogen-rich stars, however, wave energy is thermalized at the base of the hydrogen-rich envelope and is likely insufficient to unbind the entire envelope. While small amounts of material may be unbound by a weak shock excited by wave heating, the one-dimensional models exhibit an inflation of the envelope as the extra thermal pressure blows a low-density “bubble” at the base of the hydrogen envelope.

However, the energy deposition can give rise to non-radial hydrodynamical instabilities that cannot be captured in any of the previous one-dimensional simulations. As mentioned above, wave energy deposition in a low-density bubble causes it to have a high thermal pressure but a low density. As it expands into the low-pressure and high-density envelope, Rayleigh–Taylor instability will occur at the interface between the bubble and the overlying envelope, strongly modifying the subsequent dynamics of the envelope’s response. It therefore becomes interesting to examine multi-dimensional simulations of the star’s response, which have never been performed in a systematic way for this process. In this work, we explore the general behavior of the envelope in response to such energy deposition and examine the aspherical effects on the pre-SN mass loss and the envelope structure.

The organization of the paper is as follows. In Section 2, we describe the hydrodynamical formalism for modeling the wave energy deposition in the stellar envelope and how we construct the initial model. Then in Section 3 we present a benchmark model that demonstrates the typical effects of wave heating in multiple dimensions. In Section 4, we examine how the mass loss process and the envelope structure change with the energy deposition and its duration. In Section 5, we discuss implications for supernovae and progenitor stars with different rates and durations of wave heating. In the Appendix, we further show how our simulations depend some of the input parameters, including the mesh resolution, the initial perturbation, and the boundaries.

2. Methods

2.1. Stellar Model

To construct the initial models for the hydrodynamics run, we first use the one-dimensional stellar evolutionary code MESA (Modules for the Experiments in Stellar Astrophysics, Paxton et al. 2011, 2013, 2015, 2017, 2019) version 8118. We evolve a $15 M_{\odot}$ star with solar metallicity, starting at the zero-age main sequence. The simulation continues until the central density approaches $10^{10} \text{ g cm}^{-3}$. Then we extract the stellar profile when the star is carrying out core O-burning and map it to our two-dimensional mesh.

In the top left panel of Figure 1 we plot a Hertzsprung–Russell diagram of the model’s evolution, and in the top right panel we plot the time evolution of the nuclear, neutrino, and surface

luminosities of the stellar model. The surface luminosity does not vary during the late-stage vigorous nuclear burning in the core, but the neutrino luminosity in general follows the nuclear luminosity. Note that the shell burning of C and Ne triggers a brief jump in the nuclear luminosity, while O-burning provides a more steady energy production. In the bottom right panel of Figure 1, we plot the density and temperature profile of the MESA profile. We model only the outer part beyond $10 R_{\odot}$ in the simulations, corresponding to $m(r)/M \sim 0.5$ at the base of the H-envelope where the wave heating is expected to take place.

2.2. Hydrodynamics

We use a two-dimensional hydrodynamics code that we previously used extensively for SN simulations. The code is designed for multiple purposes and has been used in simulations of Type Ia SNe (Leung et al. 2015; Leung & Nomoto 2018, 2020), electron capture SNe (Leung & Nomoto 2017, 2019; Zha et al. 2019b; Leung et al. 2020) and accretion-induced collapse (Leung et al. 2019b; Zha et al. 2019a). The code utilizes the fifth-order shock-capturing weighted essentially non-oscillatory (WENO) scheme (Barth & Deconinck 1999) and the five-step third-order non-strong-stability-preserving Runge–Kutta scheme for time discretization (Wang & Spiteri 2007) of the Euler equations. In this work, we consider the equatorial plane of the star in polar coordinates (ρ, θ) . This allows the use of a reflective boundary in the radial direction and a periodic boundary in the θ -direction. To perform the simulations in a computationally feasible time range, we run the simulations in a single quadrant.

To close the equations, we use the Helmholtz equation of state (Timmes et al. 2000). This consists of contributions from electron gas with arbitrary degeneracy, ions in the form of an ideal gas, photons in the Planck distribution, and electron–positron pairs. We use a reflective boundary for the radial inner boundary, and a free-flow boundary for the radial outer one. When the energy deposition is strong, the fluid near the inner boundary can expand significantly, causing mass flow outward. In that case, we provide additional mass to the innermost grid cells such that the outflow mass is balanced by the additional mass, as it would be in a real star by upwelling material. Then, we inject the corresponding gravitational energy to the system to maintain energy conservation and adjust the mass cut value. This ensures that the total mass and energy, including both the hydrodynamical grids and the mass cut, are conserved as a whole.

2.3. Energy Deposition

Below we describe the changes to the code in order to accommodate the wave heating physics. We consider a wave luminosity emerging from the core, $L_{\text{wave},0}$, that propagates into our computational domain and then dissipates into heat. We model only the heat dissipation and not the waves themselves. In each time step, we compute how much energy is deposited at each of the computational mesh points by comparing the maximal luminosity $L_{\text{max}} = 2\pi r^2 \rho c_s^3$ and the local L_{wave} , which decreases with radius as wave energy is converted into heat. When $L_{\text{max}} > L_{\text{wave}}$, no change in L_{wave} is made. Otherwise, the new L_{wave} is computed by solving (see, e.g., Landau & Lifshitz 1959; Ulmschneider 1970; Mihalas & Mihalas 1984; Fuller & Ro 2018

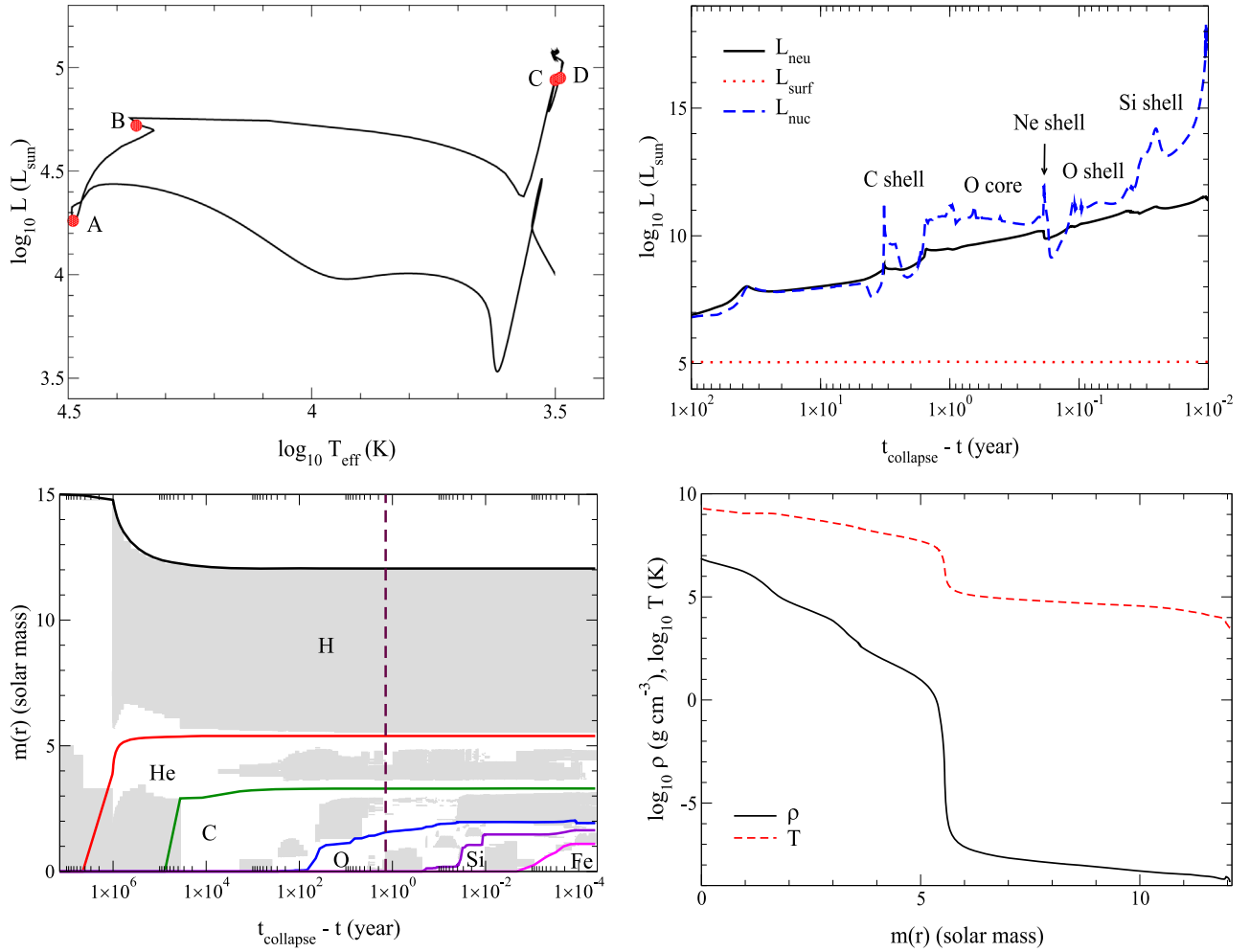


Figure 1. Top left: HR diagram of our $15 M_{\odot}$ stellar model. The letters A–D stand for the onset and end of H-burning (A and B) and He-burning (C and D) respectively. Top right: nuclear, neutrino, and surface luminosities of the star against time. Bottom left: Kippenhahn diagram of the model. Colored lines are the mass coordinates of the He, C, O, Si, and Fe cores. The vertical dashed line indicates the moment when the snapshot is taken for the hydrodynamics simulation. Bottom right: density and temperature profiles at the onset of the O-burning phase.

for derivations)

$$\frac{dL_{\text{wave}}}{dm} = \frac{\gamma + 1}{3\pi} \omega c_s^2 \left(\frac{L_{\text{wave}}}{L_{\text{max}}} \right)^{3/2}. \quad (1)$$

This formula is appropriate for waves that gradually steepen to form weak shocks (i.e., the post-shock pressure only slightly exceeds the pre-shock pressure), which occurs when L_{wave} is slightly larger than L_{max} . As discussed in Fuller & Ro (2018), the weak shock damping prevents the waves from steepening into strong shocks with $L_{\text{wave}} \gg L_{\text{max}}$, so the approximation of Equation (1) is good throughout most of the wave energy deposition region.

The relative change $\Delta L_{\text{wave}}/L_{\text{wave}}$ can be very steep for a high value of L_{wave} . We smooth the energy deposition by hand to a mass with a minimum of $m_{\text{dep},\min} = 0.1 M_{\odot}$, which ensures that the process of energy deposition is resolved at the current resolution. To do this, the energy along each ray with a given θ is smoothed over a mass $m_{\text{dep},\theta} = 0.1 M_{\odot}/N_{\theta}$, where N_{θ} is the number of grid points along the θ -direction. In each step, we search along a constant θ -direction for the transition position (r_0, θ_0) where $L_{\text{max}} = L_{\text{wave}}$. Then we integrate outward to look for the outer radius r_1 so that the accumulated mass

$\int_{r_0}^{r_1} \text{vol}(r, \theta_0) \rho(r, \theta_0) = m_{\text{dep},\theta}$. The local energy deposition in each grid cell is the mass of the cell divided by $m_{\text{dep},\theta}$.

2.4. Initializing Hydrodynamics

After evolving the stellar model, we take one snapshot during core O-burning, and map the density and pressure into our 2D simulation. The profile from the stellar evolution code obeys hydrostatic equilibrium. However, during mapping from the Lagrangian MESA mesh to the Eulerian simulation mesh, slight departures from hydrostatic equilibrium can be introduced. For the inner boundary, we chose a mass cut of mass $\sim 5.5 M_{\odot}$ with a radius $\sim 7.5 \times 10^{11}$ cm, near the base of the hydrogen envelope and below the initial wave heating region. We use a uniform 1500×30 grid with a radial grid size of 1.5×10^{11} cm and angular grid size of 3° .

In Appendix A, we further study how our model achieves hydrostatic equilibrium after it is mapped to our hydrodynamics model. While radial motion and changes to the density profile do occur, they are smaller than those caused by the wave heating that we examine below. Additionally, convection is not present in the initial model, which may underestimate the energy transport at early times if convective flows can help channel the deposited energy away.

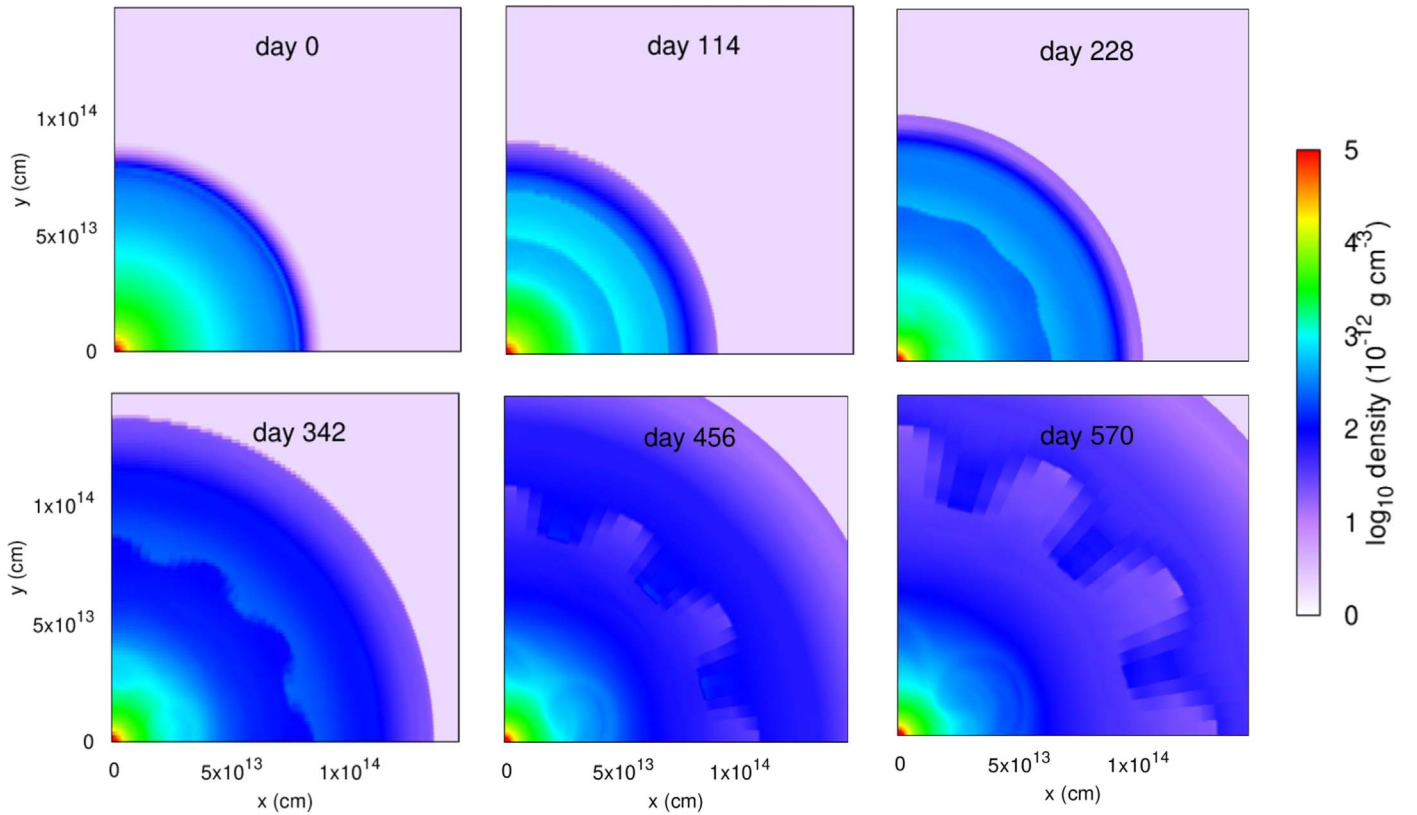


Figure 2. Density color plots of our benchmark model (Model 4 from Table 1, with $L_{\text{wave}} = 3 \times 10^6 L_{\odot}$ for a duration of 120 days) at 0, 114, 228, 342, 456 and 570 days after the onset of energy deposition. The box size of all panels is fixed at $(1.5 \times 10^{14}, 1.5 \times 10^{14})$ cm for comparison.

The initial profile is spherically symmetric, so we add density perturbations in the form $\delta\rho(r, \theta) = \alpha\rho \sin(12\theta)\sin(br/R)$. We choose $\alpha = 0.01$ in this work. In Appendix C we demonstrate that the exact value of α does not change our results. The density perturbation is added to mimic the inherent density fluctuations due to convection, and aims at seeding the growth of non-radial instabilities. The value b is chosen such that the total mass is conserved globally and along each radial direction. This prevents global motion of the star in any specific direction.

3. Benchmark Model

Here we focus on this $15 M_{\odot}$ benchmark model, and in Section 5 we further discuss the dynamics based on models of different progenitor masses.

3.1. Hydrodynamical Response of Benchmark Model

When the energy deposition starts, the heated region is usually within a narrow band in radius near the bottom of the simulation domain. As outlined in the previous section, the deposition region is smoothed along $0.1 M_{\odot}$ starting from the innermost grid point with energy deposition. For our benchmark model the heating rate is set to $3 \times 10^6 L_{\odot}$ and lasts for 120 days. In Figure 2, we show density color plots of the benchmark model at different time slices to show how the star expands and contorts due to energy deposition. The energy deposition creates a layered structure, due to weak shocks propagating through the envelope, as seen on day 114. Like the 1D models, the 2D models exhibit a “bubble” of lower density within the envelope, but with a weaker density inversion. At day 114, the bubble surface is near 6×10^{13} cm but expands

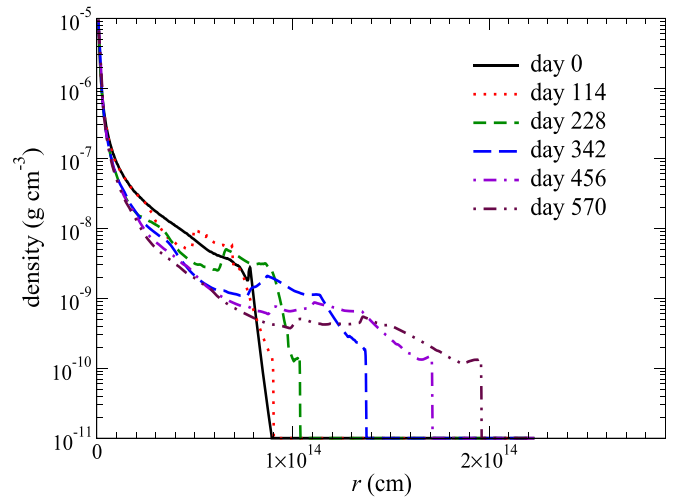


Figure 3. The angle-averaged density profiles of the benchmark model at selected times after the start of energy deposition.

outward, and by day 228, the bubble surface is wavy due to the density perturbations introduced in our initial conditions. The heating ceases after day 120, but the star does not expand significantly until after day ~ 200 , when the heat-induced pressure wave reaches the stellar surface. The core also develops non-radial structures due to non-radial instabilities and flows driven by the heating.

We plot in Figure 3 the angle-averaged density profiles of the benchmark model at selected times to further analyze the density and velocity evolution of the ejecta. The energy

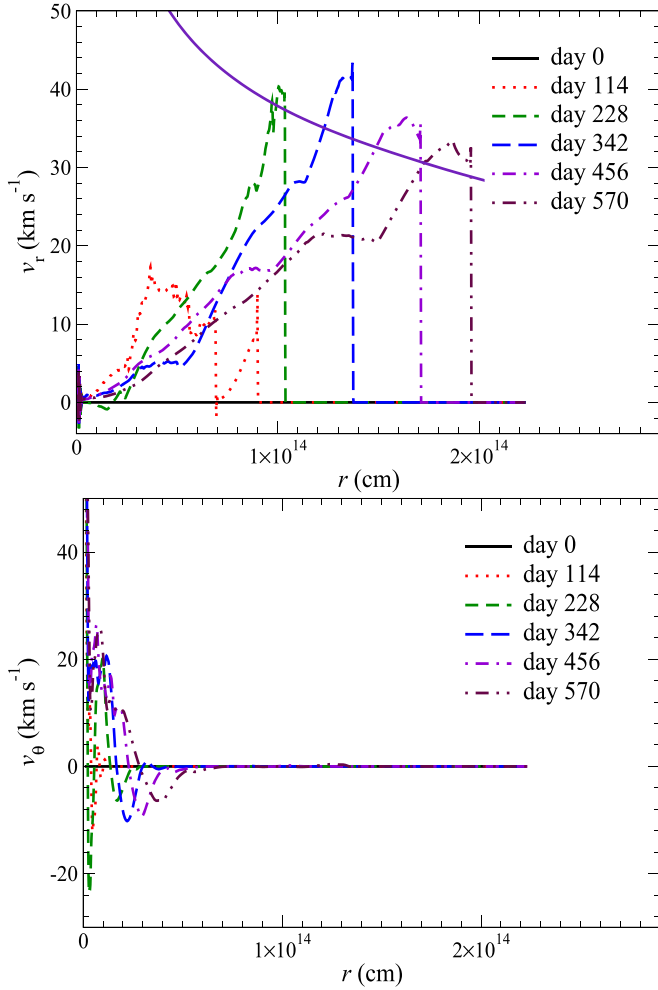


Figure 4. Top: the angle-averaged v_r profiles of the benchmark model at selected times. The solid purple line corresponds to the escape velocity defined by $v_{\text{esc}} = (2GM_{\text{int}}/r)^{1/2}$, where M_{int} is the mass enclosed within a radius r . Bottom: the angle-averaged v_θ profiles.

deposition takes place near the core at $\sim 10^{13}$ cm, driving a density inversion that propagates outward. The density difference can be a factor of ~ 3 between the minimum value in the trough and the peak. The angle-averaged density inversion gradually smooths out as the star expands, due to the growth of the Rayleigh–Taylor instability from the seed perturbations added to the model, which create the wavy patterns seen in Figure 2.

In the left panel of Figure 4, we plot the angle-averaged radial velocity profile of the benchmark model. The energy deposition occurring in the first 120 days drives expansion of the envelope, with internal velocities $\sim 15 \text{ km s}^{-1}$. When this velocity/pressure wave reaches the surface, where the density is small, it steepens into a shock to trigger a rapid expansion of the envelope. The velocity can be as high as $\sim 40 \text{ km s}^{-1}$, near the escape speed of the star’s surface. As the envelope expands, it slows down due to gravity, approaching $\sim 30 \text{ km s}^{-1}$ at 570 days after the start of energy deposition.

To further understand the asphericity of the ejecta, we also plot in the bottom panel of Figure 4 the angle-averaged angular velocity snapshots. Most of the star has a smaller angular velocity than the radial velocity, but the angular velocity reaches $\sim 20 \text{ km s}^{-1}$ within the innermost 2×10^{13} cm. The direction of the angular flow changes with both radius and time

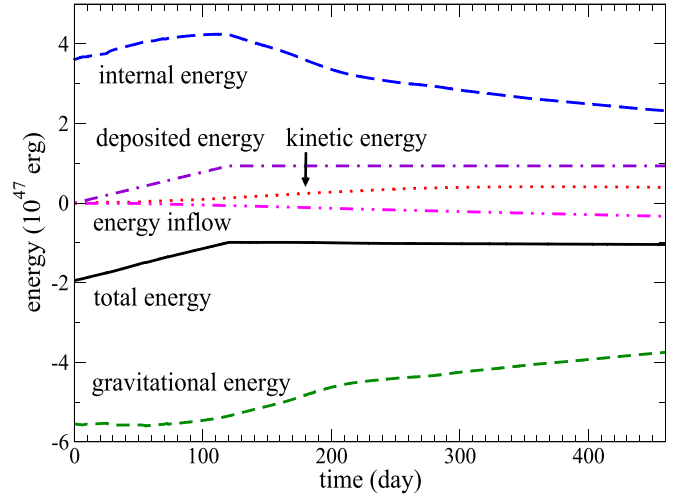


Figure 5. Energies as a function of time for the benchmark model. The energy components include kinetic energy (red dotted line), gravitational energy (green dashed line), internal energy (blue long-dashed line), deposited energy (purple dotted-dashed line), energy inflow (magenta dotted-dotted-dashed line), and total energy (black solid line).

due to its turbulent nature. Beyond $\sim 5 \times 10^{13}$ cm, there is no observable motion in the angular velocity.

In this model, there is no direct mass ejection. The outer boundary at 2.3×10^{14} cm is sufficiently large to contain all matter during the simulation. Only the outer layers of the star achieve velocities close to the escape velocity. While pressure gradients may still provide extra acceleration, the sub-escape velocities of inner layers suggest that the net mass ejection will be low. Besides, after the O-burning has started, it takes ~ 1 yr before the final collapse takes place, so there might not be sufficient time for any matter to escape before the final collapse.

Finally, we examine the energy budget of the benchmark model. In Figure 5, we plot the different components of energy as a function of time. The total energy grows linearly in the first 120 days due to the deposited energy in the model. Note also the small negative energy inflow due to the gravitational potential energy of mass added to the system as described in Section 2. Examining the trends in gravitational energy and internal energy, we see that the star does not significantly expand in the first 100 days, but then expands noticeably, lowering the gravitational energy. The early growth and subsequent decline of internal energy show that the system first stores the deposited energy in thermal energy, and later converts this into kinetic energy, which is then converted into gravitational energy as the star expands outward. We also note that the internal energy eventually decreases below its initial value, reflecting the nearly adiabatic losses during envelope expansion.

4. Dependence on Wave Heating Parameters

In the previous section, we examined how the envelope responds to wave energy deposition for a benchmark model. Here, we extend our study to examine how these properties depend on the rate and duration of energy deposition. Table 1 lists parameters of the models we have run, where the benchmark model is Model 4. We also remark that another way to compare the model is by the total energy deposited. In this sense, Models 1 and 3 form the “low-energy models”

Table 1
Parameters and Energetics of the Models Studied in this Work

Model	L_{wave}	Duration	E_{dep}	E_{ini}	E_{fin}	Unbound Mass	Remarks
Unit	($10^7 L_{\odot}$)	(day)	(10^{47} erg)	(10^{47} erg)	(10^{47} erg)	(M_{\odot})	
1	0.1	120	0.398	−1.948	−1.586	0.04	
2	0.1	360	1.195	−1.948	−1.033	1.3	
3	0.3	40	0.398	−1.948	−1.585	0.01	
4	0.3	120	1.195	−1.948	−1.055	0.26	
5	0.3	360	3.585	−1.948	0.686	3.9	
6	1.0	40	1.195	−1.948	−1.153	0.18	
7	1.0	120	3.585	−1.948	0.351	5.8	
4a	0.3	120	1.195	−1.948	−1.049	No	Seed = 0.1
4b	0.3	120	1.195	−1.948	−0.975	No	Seed = 0.001
4c	0.3	120	1.195	−1.948	−1.053	No	$M_{\text{dep}} = 0.05 M_{\odot}$
4d	0.3	120	1.195	−1.948	−1.046	No	$M_{\text{dep}} = 0.2 M_{\odot}$
4s	0.3	120	1.195	−1.948	−0.685	No	No initial seed

Note. L_{wave} is the wave heating rate, Duration is the length of wave energy deposition, and E_{dep} is the total energy deposited. E_{ini} and E_{fin} are the initial and final total energies of the envelopes in the simulations.

(LEMs); Models 2, 4, and 6 form the “medium-energy models” (MEMs); and Models 5 and 7 form the “high-energy models” (HEMs).

4.1. Dependence on Total Wave Heat

We first study how models with the same total deposited energy behave, from which we can extract some general observations about the effects of wave energy deposition.

4.1.1. Hydrodynamics of LEMs

In Figure 6, we plot in the upper (lower) panel the density profiles of Model 1 (3) taken from the LEMs. In Model 1, which has a lower L_{wave} , the star shows a regulated expansion. A density inversion (like that shown in the benchmark model) develops at 8×10^{13} cm at day 114 and slowly propagates to 2×10^{14} cm by day 570. The density contrast across the inversion nearly stays fixed at roughly a few times the minimum density, while the sharp density gradient at the surface remains. In Model 3, the expansion proceeds steadily without forming a density inversion. A strong shock does not form in either case, leaving a sharp density gradient at the surface, and all material in the star remains gravitationally bound.

Figure 7 shows the radial velocity profiles of the LEMs. In Model 1, the initial energy deposition triggers a pulse-like velocity profile at day 114 with a peak velocity of $\sim 30 \text{ km s}^{-1}$ at day 228. The whole star is gravitationally bound, including the shock-heated surface. Model 3 shows an erratic velocity profile characterized by shocks at early times, which can be seen at $3, 5, 7$, and 9×10^{13} cm at day 114. After the shocks reach the surface, the star exhibits nearly “homologous” expansion in the sense that the expansion velocity is roughly proportional to radius. Again the velocity is too low to escape the star directly. The surface velocity is only 15 km s^{-1} at the end of the simulation.

These two models suggest that the actual changes in the density and velocity profiles are almost negligible in the

low-energy regime. The heat triggers moderate expansion but no major restructuring of the density profile.

4.1.2. Hydrodynamics of MEMs

In Figure 8 we plot the density profiles of two models with the same energy input as the benchmark model, with $E_{\text{dep}} = 1.195 \times 10^{47}$ erg, but at a low heating rate of $10^6 L_{\odot}$ for 360 days (Model 2) and at a high heating rate of $10^7 L_{\odot}$ for 40 days (Model 6). The lower energy deposition in Model 2 creates a density inversion that mildly accelerates with time as the density contrast approaches the surface. The density difference can be a few times higher than the minimum density at the trough. The star smoothly expands to $\sim 1.9 \times 10^{14}$ cm. In Model 6, no significant density inversion develops in the whole simulation, just a small one near the surface. The stellar density profile is mostly monotonically decreasing and expanding, signifying a smooth expansion. The outer layers stagnate at the end of the simulation, suggesting that the star’s expansion slows down, with all of its matter remaining bound.

In Figure 9, we plot the velocity profiles of the MEMs. Similar to the density profiles, the velocity profiles also show interesting differences between the two models. Model 2 with a low heating rate does not show deceleration, and the star reaches nearly homologous expansion at the end of simulation. Model 6 shows almost the opposite behavior. The energy injection creates a two-peak shock structure at day 114, with the inner shock traveling faster than the outer. The shocks merge into a stronger shock at day 228, which reaches above 60 km s^{-1} , almost 50% higher than Model 2, despite the same total energy deposited. However, the expansion is not sustained by further heating, and the surface velocity drops by half and reaches $\sim 30 \text{ km s}^{-1}$ at the end of the simulation.

4.1.3. Hydrodynamics of HEMs

We next examine the HEMs, Models 5 and 7, which have a higher deposited energy of 3.585×10^{47} erg. Figure 10 shows that the density profiles are drastically altered by the large energy deposition. Both models develop large density

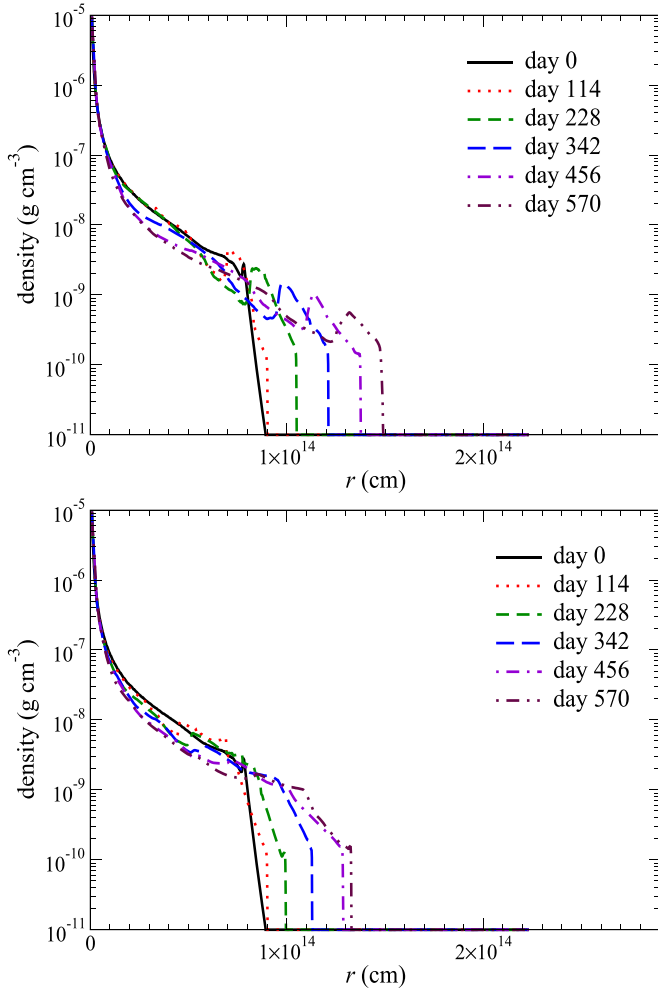


Figure 6. The angle-averaged density profiles of low-energy models ($E_{\text{dep}} \sim 4 \times 10^{46}$ erg) with Model 1 (top) and Model 3 (bottom). The corresponding heating rates are $10^6 L_{\odot}$ for 120 days in Model 1 and $3 \times 10^6 L_{\odot}$ for 40 days in Model 3.

inversions as material in the inner envelope is lifted outward. In Model 5, which has a lower L_{wave} , the density profile is flattened, with a density peak near 6×10^{13} cm at day 114 that propagates to nearly 2×10^{14} cm by day 570. In Model 7, the higher heating rate drives a stronger shock that expels material to larger radii. At day 456, the outer layers of the star reach the outer boundary of the simulation at $\sim 2.3 \times 10^{14}$ cm.

In Figure 11, we plot the velocity profiles of Models 5 and 7 from the HEM series. Model 5 shows that the star can still expand rapidly with a moderate L_{dep} but with a long duration. The velocity profile features a strong two-peak structure at intermediate times but approaches homologous expansion at late times. The outer layers asymptotically approach a velocity $\sim 40 \text{ km s}^{-1}$ larger than the escape speed. The inner layers slow down with time, developing a complex turbulent structure in the core.

Dynamical features accompany the expansion in the velocity profiles of Model 7. When the strong shock breaks out from the surface of the star around day 228, the velocity peaks at 70 km s^{-1} , compared to the local escape velocity of $\sim 40 \text{ km s}^{-1}$. Afterwards, the ejecta slows down but can still escape. Turbulent motion persists in the inner part of the star. The outer layers of the ejecta reach the outer boundary of the simulation as shown in the profile at day 456. At the end of the run, the star approaches homologous expansion.

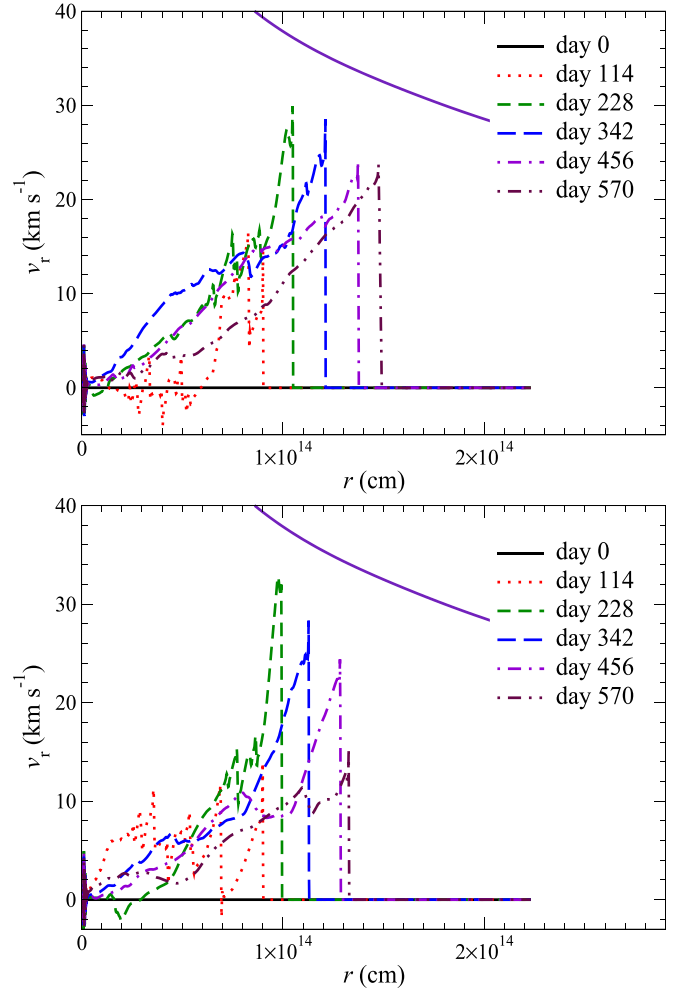


Figure 7. Top: the angle-averaged radial velocity profiles of low-energy models ($E_{\text{dep}} \sim 4 \times 10^{46}$ erg) with Model 1 (top) and Model 3 (bottom).

4.2. Dependence on Wave Heating Rate and Duration

In this section, we discuss general differences between models with the same wave heating rate but different durations, or vice versa. The duration is determined by the lifetime of the core burning. The duration of the advanced burning, such as O-burning, generally decreases with stellar mass. The exact heating rate is also unclear because there is significant uncertainty in the wave luminosity generated by the convective core, but it is expected to increase for more massive stellar cores. Here, we explore the consequences of the variation of these values for the mass ejection process.

We examine how L_{wave} affects the evolution of the velocity profile by analyzing the three models with a heating duration of 120 days: Model 1 (LEM), Model 4 (MEM), and Model 7 (HEM). The energy deposition rate significantly affects how the star expands and how the star ejects mass. A lower L_{wave} makes the star expand but with no mass ejection. Higher values of L_{wave} can drive stronger shocks that lead to mass ejection from the surface. Only Model 7 with $L_{\text{wave}} = 10^7 L_{\odot}$ exhibits significant mass ejection due to wave heating. The larger energy deposition of the HEM not only makes the star expand faster, but it also creates a prolonged trough in the density profile inside the star. In contrast, the LEM exhibits very little internal motion or mass ejection in its velocity profile.

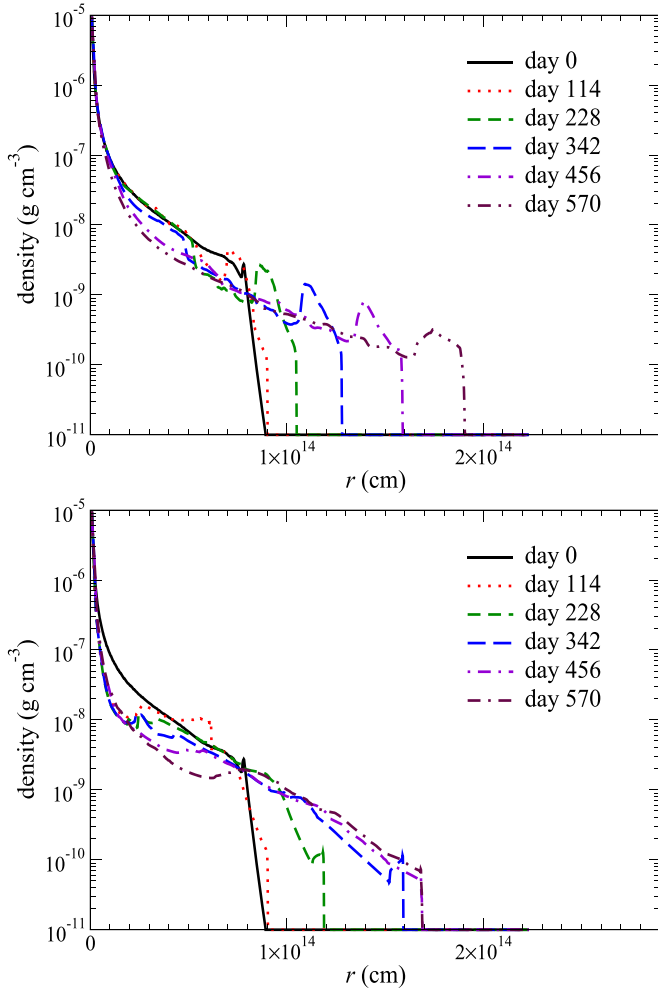


Figure 8. Top: same as Figure 6 but for the medium-energy models ($E_{\text{dep}} \sim 1 \times 10^{47}$ erg) with Model 2 (top) and Model 6 (bottom). The two models and the benchmark model share the same amount of deposited energy, but with a low heating rate of $10^6 L_{\odot}$ for 360 days in Model 2 and a high heating rate of $10^7 L_{\odot}$ for 40 days in Model 6.

We identify significant differences in the density and velocity structures between models with different heating rates. Models with low but sustained heating rates exhibit more steady expansion, with a small density inversion forming as the outer layers are gradually lifted outward by the expanding inner layers. Due to the low heating rate, no strong shock wave is excited, and matter is not shock-accelerated near the surface. We refer to this as a “bubble” phenomenon. In contrast, a larger heating rate excites a stronger shock that accelerates the surface layers outward, creating a low-density tail of material above the previous location of the photosphere, with a much smaller density inversion interior to this tail. We refer to this as a “bomb” phenomenon. Thus, low heating rates create a “bubble” phenomenon, while high heating rates (i.e., a heating timescale shorter than the local dynamical timescale) create a “bomb” phenomenon.

4.3. Global Comparison of Mass Loss

In Figure 12, we plot the total ejecta mass against time for the models presented. The ejecta mass is defined by the integrated mass elements when the sum of the local kinetic

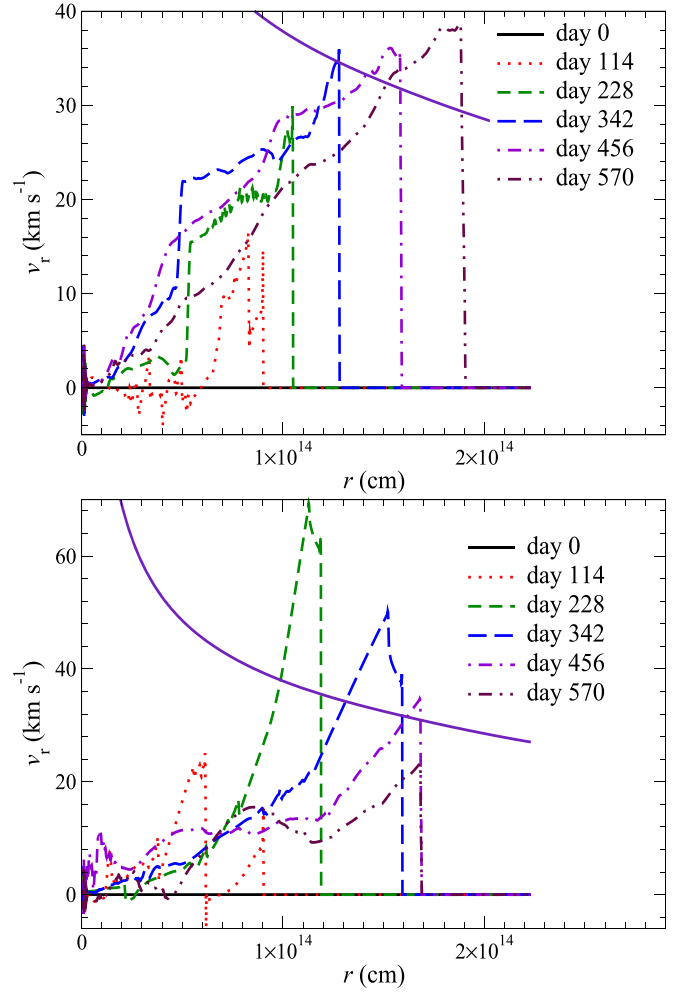


Figure 9. Top: same as Figure 7 but for the medium-energy models with Model 2 (top) and Model 6 (bottom).

energy, internal energy, and potential energy is positive. This quantity is therefore time-dependent as demonstrated in previous sections. The seven models can be characterized into three groups based on the total energy deposition: LEMs exhibit little to no mass loss, MEMs exhibit moderate amounts of mass loss, and HEMs exhibit large amounts of mass loss. For LEMs (Models 1 and 3), there is effectively no ejected mass because the escape mass is as low as $\sim 10^{-2} M_{\odot}$. The MEMs (Models 2, 4, and 6) show an ejected mass that is roughly an order of magnitude higher at $0.5\text{--}1.5 M_{\odot}$. Finally, in HEMs (Models 5 and 7), the ejected mass reaches asymptotic values of $4\text{--}6 M_{\odot}$, where the whole envelope mass is also $\sim 6 M_{\odot}$.

The heating rate also affects the evolution of the ejected mass. Unsurprisingly, models with the largest heating rates (Models 6 and 7) show the fastest initial increase in unbound mass, while models with the lower heating rates require a longer time for any mass to accumulate enough energy to escape. Between models with the same energy deposition, lower heating rates with longer durations generally produce larger ejecta masses.

4.4. Global Comparison of Deposition Radius

Here we compare the positions where the acoustic waves deposit energy. In Figure 13, we plot the position of the energy

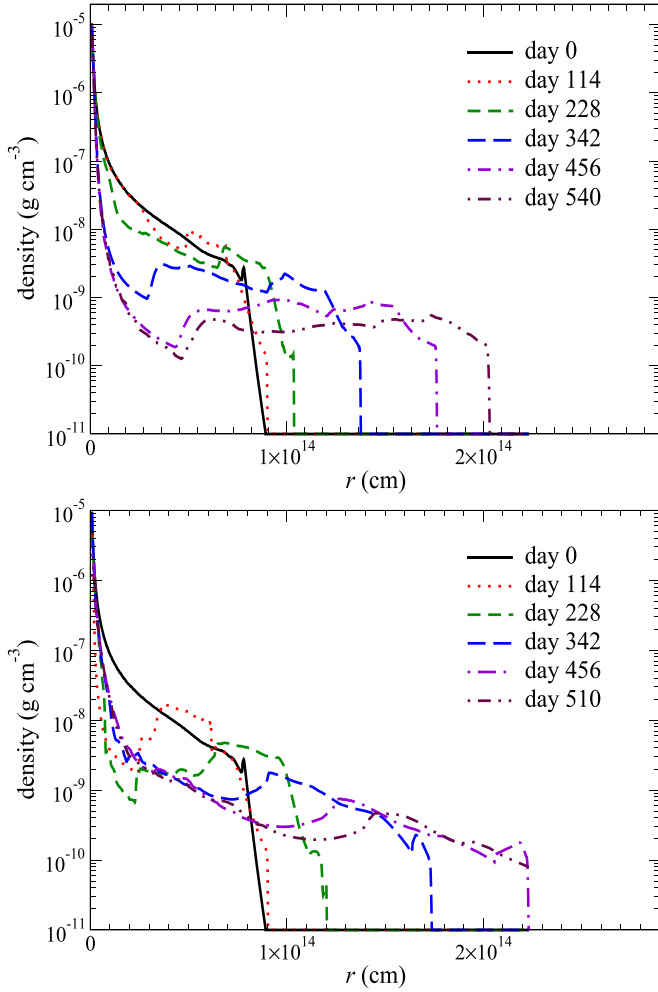


Figure 10. Top: same as Figure 6 but for high-energy models ($E_{\text{dep}} \sim 4 \times 10^{47}$ erg) with Model 5 (top) and Model 7 (bottom). The two models have heating rates of $L_{\text{wave}} = 3 \times 10^6 L_{\odot}$ (Model 5) and $9 \times 10^6 L_{\odot}$ (Model 7).

deposition against time for the models presented. The sharp drop in all curves occurs when heating abruptly shuts off. We see that models with a lower L_{dep} have their energy deposition at larger radii, which vary from $\sim 5 \times 10^{13}$ cm in Models 1 and 2 down to 2×10^{12} cm for Model 7. As the acoustic waves deposit their energy only when the maximum wave energy flux is exceeded (Equation (1)), a lower energy deposition rate requires a lower density and sound speed to match this criterion, so the heating occurs at larger radii. The roughly constant heating radius in Models 1–5 before day 100 suggests that the wave energy does not strongly alter the stellar structure in the wave heating region during this time. The trends in the heating radius are correlated with L_{dep} , because the wave heat causes the inner envelope to expand and decrease in density, causing the heating radius to move inward. This happens almost immediately for the largest heating rates. As seen in Models 5 and 7, the recession of the deposition sphere can reduce its size by almost an order of magnitude.

4.5. Global Comparison of Energy

At last, we compare the total energy as a function of time among all models and plot this in Figure 14. Unsurprisingly, the final energy is mostly determined by the total acoustic wave

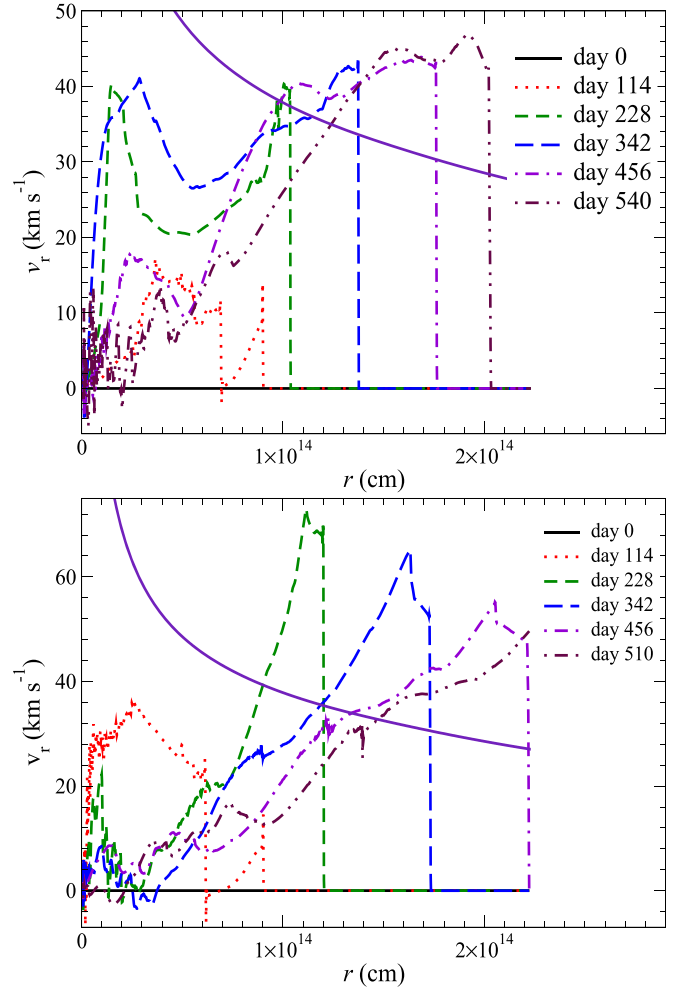


Figure 11. Top: same as Figure 7 but for high-energy models with Model 5 (top) and Model 7 (bottom).

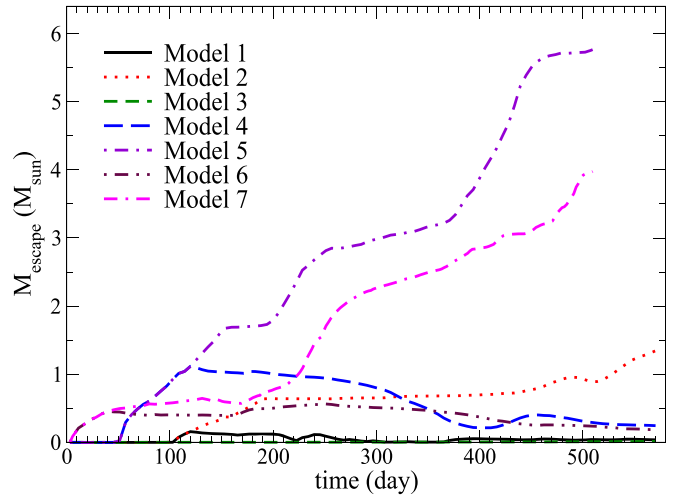


Figure 12. The time evolution of the ejecta mass of models presented in this work. The ejecta mass is defined by the total mass of matter where the sum of the local kinetic, internal, and potential energies is positive.

energy deposition. Note that only Models 5 and 7 finish with positive total energy, implying large amounts of unbound material, as verified by the results in Figure 12. However, as the star expands, extra contributions of energy emerge due to the energy content of inflowing/outflowing matter across the

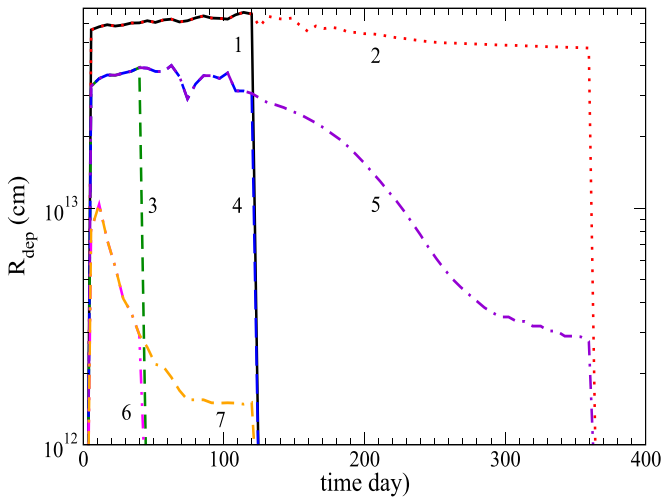


Figure 13. The time evolution of the energy deposition radius for the models presented in this work. For each model, the deposition radius falls to zero when we turn off wave heat. In models with high heating rates (Models 5 and 7), the deposition radius moves inward as the density near the base of the simulation decreases due to wave heating.

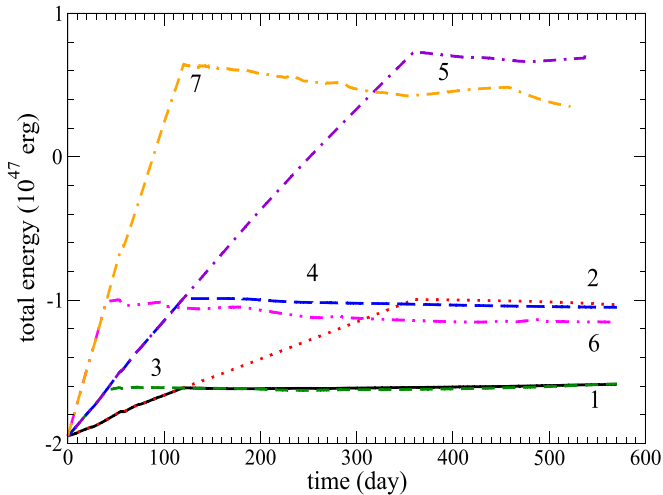


Figure 14. The time evolution of the total energy for the models presented in this work.

simulation boundaries, so the final energy in the simulation is not merely the sum of the initial energy and the heating energy.

This is not just an artifact of the simulations, because mass in a real star will generally flow from below the wave heating region to above it, changing the net energy content of the envelope. This effect is negligible for models with lower L_{dep} , due to a smaller contribution from material flowing across the boundaries. Models with larger heating rates drive material away from the inner boundary, causing more matter to flow into the simulation domain from the inner boundary, which advects negative gravitational energy into the simulation domain.

In Model 5, there is a mild increase of energy between days 400 and 450. This is the period when the rapid expansion creates an energy discontinuity near the isothermal outer layer, which is set to be at the minimum temperature allowed in the simulation (~ 3000 K). When the discontinuity passes across this region, fluid elements can be cooled below the minimum temperature. In this code we choose to stick with

thermodynamic consistency instead of energy consistency, so the missing energy between the actual temperature and the temperature floor is added into the system. Since this only alters the total energy budget by about 1%, we do not believe it qualitatively affects our conclusions.

5. Discussion

5.1. Pre-supernova Mass Loss in Stars of Other Masses

In general, the outburst process depends strongly on the wave excitation in the core, in addition to the properties of the envelope, and both core and envelope should be evolved together for robust estimates. Fortunately, most red supergiant envelopes have very similar, nearly polytropic structures. The envelope masses are also similar, $\sim 7 M_{\odot}$, since more massive stars have more of their mass in their cores, and lose more envelope mass by winds. In contrast, stars of different mass have very different wave heating rates and heating durations (Shiode & Quataert 2014). Hence, in our parameter study, lower values of L_{wave} for longer durations are more representative of low-mass stars, while higher values of L_{wave} for shorter durations are more representative of high-mass stars. Different burning phases behave similarly: carbon shell burning can be much longer ($\sim 10^2$ yr) but the wave luminosity is correspondingly smaller. Silicon burning generates much larger wave fluxes but only lasts days, so the envelope does not have time to respond (Fuller et al. 2015).

It is possible that other processes occur in some stars, such as convective shell mergers. These would spur intense nuclear burning and vigorous convection (Meakin & Arnett 2006; Collins et al. 2018; Yadav et al. 2020), driving very large wave fluxes into the envelope. Another scenario is that the core dynamo amplifies the magnetic field in the convective shells near the core, which could also generate waves and lead to energy deposition near the surface (Soker & Gilkis 2017). While we do not investigate such processes here, an uncommon subset of stars could generate wave fluxes much greater than our fiducial estimates.

5.2. Appearance of Wave-driven Outbursts

Our simulations do not include radiative transfer and cannot predict the detailed appearance of wave-driven pre-SN outbursts. From the 1D models of Fuller (2017), the photometric signal of a pre-SN outburst in a red supergiant is likely dominated by shocks propagating up to the photosphere after short but intense periods of wave heating, such as the core neon burning phase. Our 2D simulations with large heating rates also launch these shocks, which are not strongly affected by non-radial instabilities. Hence, we expect that the observable features of pre-SN outbursts are captured reasonably well by 1D models. When the outburst takes place in a binary system, the accretion of the ejected matter by the companion star might also produce a bright event (McIey & Soker 2014; Danieli & Soker 2019).

5.3. Envelope Asphericity

In this work, we have extensively computed two-dimensional models showing how the wave heating generates asphericity and drives mass loss. In Figure 15, we further demonstrate how the asphericity develops at late times. We examine Models 2 and 6, finding that both models are spherical

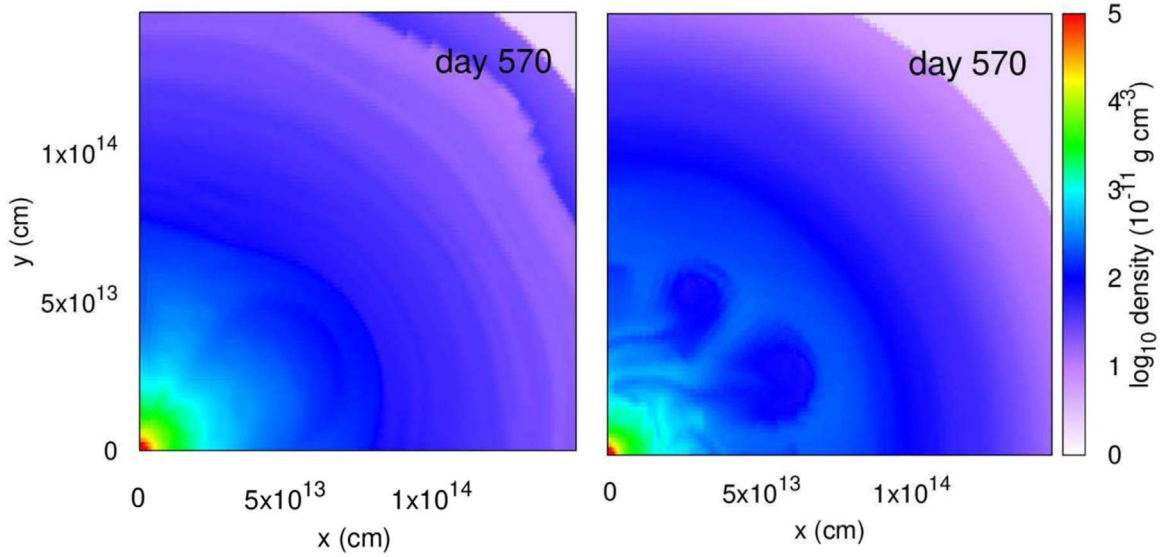


Figure 15. Density distributions of Model 2 (left) and Model 6 (right) at the end of the simulation. The two models share the same total energy deposition of $\sim 1.2 \times 10^{47}$ erg, but with $L_{\text{wave}} = 10^6 L_{\odot}$ for 12 months in Model 2 and $L_{\text{wave}} = 10^7 L_{\odot}$ for 4/3 months in Model 6.

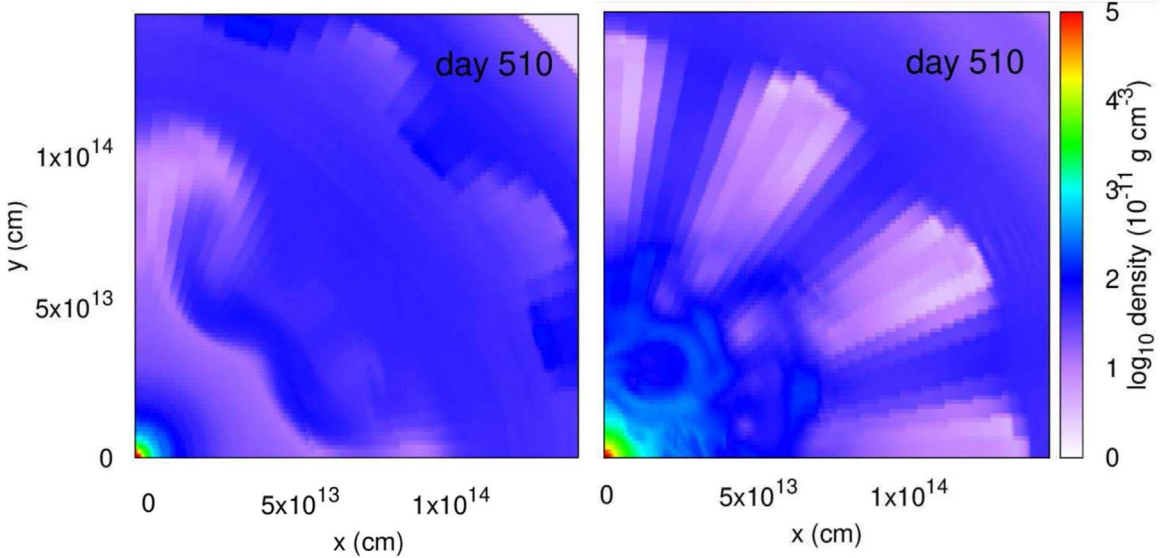


Figure 16. Density color plots of Model 5 (left) and Model 7 (right) at the end of the simulation. The two models share the same total energy deposition of $\sim 3.7 \times 10^{47}$ erg, but with $L_{\text{wave}} = 3 \times 10^6 L_{\odot}$ for 12 months in Model 5 and $L_{\text{wave}} = 10^7 L_{\odot}$ for 4 months in Model 7.

to a good approximation. However, notable turbulence is driven within the middle of the envelope, which is especially evident at radii around 5×10^{13} cm. These structures are much more pronounced in Model 6, likely because the larger heating rate (but shorter duration) fuels more expansion of the inner envelope, generating stronger Rayleigh–Taylor instability. Furthermore, the density profile in Model 2 shows observable “wrinkles,” though it is not yet clear if these features are real or numerical artifacts. For LEMs and MEMs, the asphericity is small, and the wave heating primarily contributes to a quasi-spherical expansion of the stellar envelope.

For comparison, we also plot in Figure 16 the density color plots of two higher energy models, Models 5 and 7. The most striking features of these models is the large-scale structure with three wavelengths per quadrant at radii around 10^{14} cm. This is clearly a consequence of the initial configuration of

the simulations, where a sinusoidal perturbation with three periods in the radial and angular directions (and an amplitude 1%) was embedded in the density profile. However, by the end of the simulation, this 1% perturbation has grown to a large amplitude, producing a variation by as much as a factor of 10 in the horizontal density fluctuations. We attribute this large amplification to rapidly growing Rayleigh–Taylor instability. Interestingly, the radial location where the instability is most prominent depends on the wave heating rate, but it is clear that higher total heat deposition allows for more growth of density perturbations. Of course, a real star would have initial density fluctuations at a variety of scales due to turbulent convection in the envelope, but these models indicate that those perturbations can be magnified by wave heating effects, potentially producing significant asphericity in the exploding star.

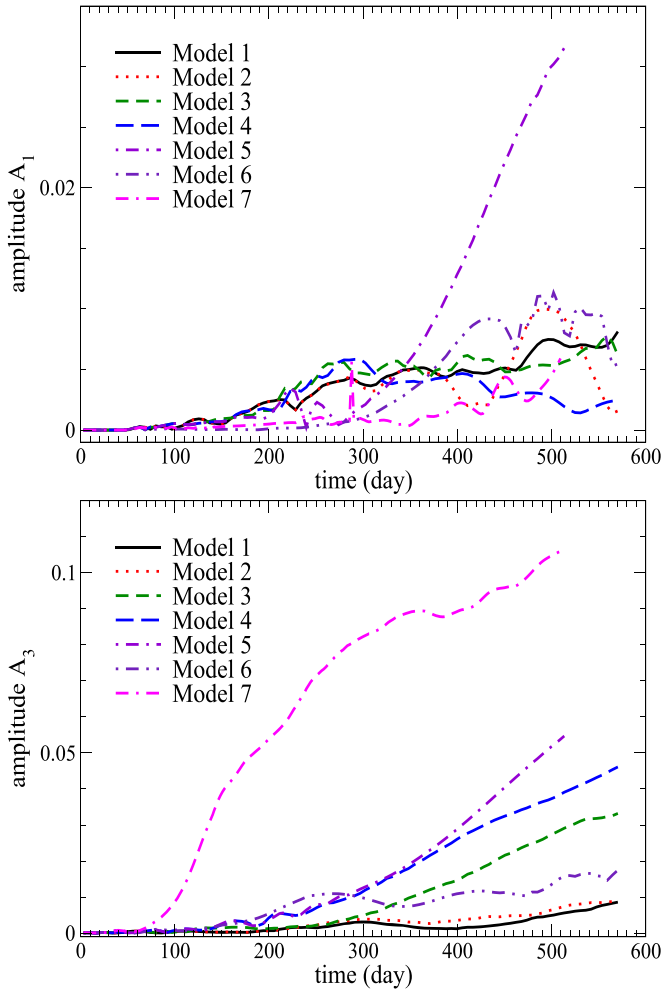


Figure 17. The time evolution of the density asphericity for all seven models presented in the main text. The asphericity is defined by $A_n = \sqrt{C_n^2 + S_n^2}$ where C_n and S_n are the cosine and sine components of the angular Fourier modes of the density profiles. The top panel shows the elongation A_1 while the bottom panel shows the A_3 component.

To quantify the level of asphericity in the models, we compute the mass-weighted asphericity via the Fourier modes

$$S_n = \frac{1}{M} \int_{R_{\text{cut}}}^R \int_0^{\pi/2} 8r^2 dr d\theta \rho \sin(n\theta). \quad (2)$$

Here, the integer n is the Fourier harmonic and M is the total mass of the star. We also compute a similar expression with C_n using $\cos(n\theta)$ as the Fourier component, and we thus define the asphericity of n th order, $A_n = \sqrt{C_n^2 + S_n^2}$.

In Figure 17 we plot the time evolution of the asphericity modes A_1 and A_3 of all seven models presented in previous sections. The $n = 3$ component is often dominant as discussed above. Comparing the two plots, A_1 is indeed smaller than A_3 by a factor of a few. The LEMs show a mild increase in asphericity, but their low values show that the stars remain nearly spherical. The MEMs show a larger asphericity that grows nearly linearly in time. The HEMs have the most significant asphericity, with the A_3 component of Model 7 reaching 10%. Despite its lower total energy deposition, Model 5 exhibits the largest value of A_1 and hence has the most

elongated structure, though the elongation only reaches $\approx 3\%$. The angular dependence of the envelope density may give rise to interesting effects for the subsequent SN and its appearance.

In Appendix B we further compare models with different initial aspherical seeds to see how this affects the star’s final asphericity, finding that the results are not strongly dependent on this choice.

5.4. Limitations of This Work

First, our simulations use a moderate resolution that is almost constant throughout the star with $\Delta x = 1.5 \times 10^{10}$ cm. This Δx is rather large compared to the mass cut, which is $\sim 7.5 \times 10^{10}$ cm. Thus, the inner features of the star might not be fully captured and may be under-resolved. This value of Δx can provide us the necessary resolution for the outer part to keep track of the smaller features due to hydrodynamical instabilities. Most such features should be produced in the outer envelope because that is the place where the density inversion is present.

Second, our simulation does not resolve the acoustic waves emitted from the core, but instead only includes a heating term to account for their energy deposition. Studying how these waves deposit heat and momentum is numerically challenging because it takes place on a short length scale and a short timescale, i.e., the wavelength and wave period. The huge number of acoustic waves leaked into the envelope provides the possibility of modeling this process statistically, namely by the recognition of L_{wave} as a time-averaged quantity. Interestingly, our results imply that the net effect is for acoustic waves to damp via weak shocks, and to convert their energy into pressure pulses with greater length scale and timescale, which then continue to propagate out until they shock again. It would be an interesting extension to resolve both the original acoustic waves and the secondary pressure pulses to see if the results differ from the treatment adopted here.

Third, we have used the Helmholtz equation of state for our computation. But for modeling the envelope, we are approaching a density close to 10^{-11} g cm $^{-3}$, which is the density floor provided by the equation-of-state table. As discussed above, the temperature would also decrease below 10^4 K if we did not impose a temperature floor. This limits us in trying to explore further how the ejecta behaves beyond day 570. In some of our more energetic models, vacuum zones develop inside the star, with a few grid cells along the same r reaching the density floor. These are not evident in the figures because the density profiles shown are angle-averaged. The large associated pressure differences begin to trigger unphysical flow. Further extrapolation to lower densities and temperatures will require an updated equation of state. Additionally, at these low densities, the matter might not be tightly coupled to the radiation field, so non-diffusive radiative transfer may be important. Furthermore, the ionization state can be out of thermodynamic equilibrium. These factors might largely complicate the computations and this extra physics will be interesting follow-up work.

The density floor is set to maintain code stability when calling the equation of state. However, the presence of such a floor also sets a minimum mass that can be resolved in our simulation. To estimate that, we consider the outermost grid cells used in our simulation, located at a radius $\sim 1.5 \times 10^{14}$ cm. Using the density floor, the minimum mass traceable by this grid is $\sim 6 \times 10^{-4} M_{\odot}$.

The corresponding masses for inner grids are smaller because the grid volume scales as $\sim r^2$. This means that the ejected mass ranging from $\sim 10^{-2}$ to $6 M_\odot$ in our models is likely well resolved by our code. For ejecta masses $\lesssim 0.01 M_\odot$, a suitable extension to even lower density below $10^{-11} \text{ g cm}^{-3}$ will be necessary. However, extending to lower densities will also require additional physical considerations, such as the validity of thermodynamic equilibrium and the inclusion of radiative processes.

Fourth, our two-dimensional simulations might underestimate small-scale turbulent features. Hydrodynamical instabilities, such as the Kelvin–Helmholtz instabilities and Rayleigh–Taylor instabilities, can extend to the Kolmogorov length scale, where the viscous nature of the fluid becomes prominent. In fact, for a three-dimensional model, the development of Rayleigh–Taylor instability can be different because the extra dimension allows an extra degree of freedom for the development of the smaller features. This phenomenon is frequently seen in large-scale eddy modeling, where two-dimensional and three-dimensional turbulent energy cascades have different directions of energy flow. However, the large-scale features reported here should be similar in the two types of simulations.

Fifth, we do not consider the effects of recombination and radiative transfer in these simulations. In our progenitor model, the outer $\approx 0.1 M_\odot$ has an optical depth $\tau \lesssim 10$, hence the assumption of high optical depth in those layers is not very good. While the approximation of radiation being in equilibrium with matter is well maintained in the rest of the star, the true ejecta mass of our less energetic models (with $M_{\text{ej}} \lesssim 0.1 M_\odot$) may be reduced if radiation can leak out before their outer layers are accelerated toward the escape speed.

The effects of recombination can also potentially affect the expansion of the envelope. Our equation of state does not include recombination energy, and the ionization temperatures of ^4He ($\sim 29,000$ K) and ^1H ($\sim 10,000$ K) overlap with the temperature range used in the simulation, meaning that partial recombination should take place during its expansion. Because of the envelope’s low binding energy, this energy contributes substantially to the energy budget, and it may drive greater envelope expansion and mass loss than predicted by these simulations. On the other hand, recombination reduces the envelope opacity, allowing thermal energy to leak out, as described above. Resolving this competition between energy deposition by recombination and energy loss by radiation will be necessary for better estimates of the mass loss and pre-SN density profile.

Sixth, in the simulations we have made approximations for the initial conditions and energy deposition. In fact, how the exact energy deposition takes place in such a thin mass slice, and how the initial convective structure can be coupled to a hydrostatic model, should be further explored.

To clarify how these limitations affect the final results, we provide more comparison tests in the appendices. In Appendix A, we study how the initial density perturbation affects the later evolution without energy deposition. In Appendix B, we examine how the choice of density perturbation affects the later evolution. In Appendix C, we further compare how our two-dimensional energy deposition differs from the one-dimensional energy deposition model previously reported in Fuller (2017). In Appendix D, we study how our choice of smearing mass for the energy deposition affects the morphology and dynamics of the ejecta. In

Appendix E, we provide further details on our coordinate system. The above tests aim at clarifying the physics necessary for a comprehensive parameter survey for our future work.

5.5. Conclusion

In this work, we study the multi-dimensional hydrodynamical response of a red supergiant envelope heated by wave energy transport from nuclear burning in the core. We extract the stellar envelope from a $15 M_\odot$ stellar model, and we inject energy similar to that expected from the wave luminosity and duration of the core oxygen burning phase. To understand sensitivity to the uncertain wave luminosity and duration, we treat the heat deposition rate and its duration as model parameters. Unsurprisingly, we find that heat deposition in excess of the envelope’s binding energy can drive large amounts of mass loss, while heat deposition lower than this threshold has a much smaller impact.

We also observe two classes of behaviors that depend on the wave heating rate. For a lower wave energy flux, the wave energy causes gradual expansion of the stellar envelope without strong mass loss, and the expansion is mostly spherical. With a high wave energy flux, the wave energy can amplify initial density asphericities and trigger uneven heating. This results in more asymmetric motion in the envelope, where the Rayleigh–Taylor instability arises, smoothing radial density inversions that occur in one-dimensional models. Larger heating rates also drive stronger shocks, expelling material above the original photosphere of the star. These low-density tails above the star’s photosphere may have important effects on the early light curves of Type II-P SNe. Such events would also likely lead to observable pre-SN outbursts.

Comparison between our two-dimensional models and spherically symmetric models shows only modest differences, mostly arising from Rayleigh–Taylor instabilities that smooth out density inversions created by wave heating. Hence, one-dimensional models are likely to yield reasonably good estimates of the unbound mass and the photometric signals produced by pre-SN outbursts in red supergiants. However, multi-dimensional models or one-dimensional models incorporating the effects of Rayleigh–Taylor instability (Duffell 2016) should be used for estimates of the pre-SN density profile.

We further discuss how the results of this work can be applied to stars of different mass. More massive stars with more vigorous convection during oxygen burning can potentially result in large enough heating rates to launch shocks that trigger observable outbursts and mass loss from the stellar envelope before the star collapses. Less massive stars with lower wave heating rates are unlikely to suffer such outbursts, except in cases where degenerate burning flashes, convective shell mergers, or a different core structure permit larger wave fluxes into the envelope. The corresponding optical signal and the implications for SNe light curves will be interesting follow-up work.

We thank Paul Duffell for useful insight regarding the simulations and results. S.C.L. acknowledges support from grants HST-AR-15021.001-A and 80NSSC18K1017. J.F. is thankful for support through an Innovator Grant from The Rose Hills Foundation, and the Sloan Foundation through grant FG-2018-10515. We thank Frank X. Timmes for his open-source subroutines for the Helmholtz equation of state and the template for the seven-isotope nuclear reaction network. We

also thank the developers of the stellar evolution code MESA for their efforts in making the code public.

Software: MESA (v8118); (Paxton et al. 2011, 2013, 2015, 2017).

Appendix A Initial Model

In building the initial model, we have used the hydrostatic model computed by the MESA code as the input. We map the one-dimensional data, containing the temperature and chemical composition as a function of the mass coordinate and radial distance, onto a two-dimensional polar grid by solving again the hydrostatic equilibrium equation for the density profile. Here we check how the initial model varies with time when there is no energy deposition. This helps us to understand whether the inner mass cut and the mapping satisfy the hydrostatic equilibrium. It also serves as a reference for how much the initial aspherical seed contributes to the initial motion.

In Figure A1 we plot in the left and right panels the density and radial velocity profiles of the test model. The initial model

is exactly the same as those used in the main text, but without any energy deposition during the simulation. From the density profiles, we can see that the star gradually relaxes to a new equilibrium that is slightly different from the initial conditions. The star mildly expands, indicated by the mild drop of the density at $(2-7) \times 10^{13}$ cm and the outward motion of the surface. By the end of the simulation, the sharp cliff in density at the photosphere, originally at 9×10^{13} cm, is partially smoothed out.

From the velocity profile, we can see that the initial conditions do create some internal motion, leading to radial velocities of ~ 20 km s $^{-1}$, which is much lower than the escape velocity at ~ 60 km s $^{-1}$. However, by comparing with the models from the main text, we can see that the motion is much smaller than in those with even low amounts of energy deposition, such as Model 3. Those models have a final radius of ~ 1.5 – 2 times the initial radius, while the test model only expands by $\sim 20\%$. Hence, we can be confident that the majority of the response in the heated models is due to the deposited energy, as opposed to artifacts of the initial conditions.

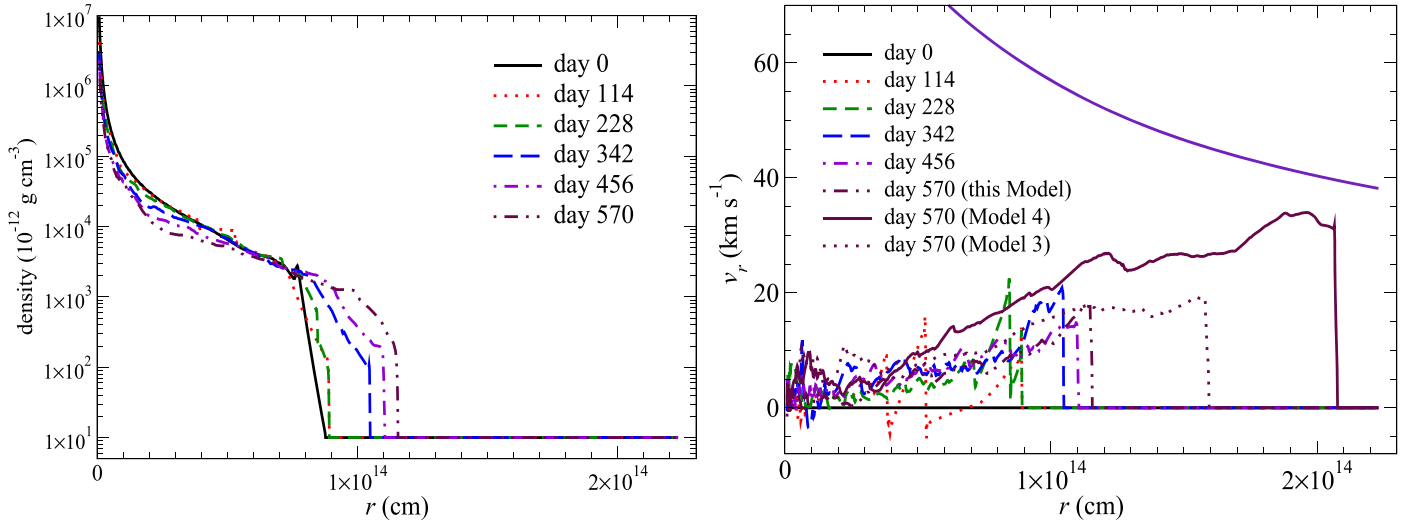


Figure A1. The angle-averaged density (left) and the radial velocity (right) of the test model without energy deposition. For comparison, we also included velocity profiles of Models 3 and 4 at the same time points. The escape velocity (purple solid line) is included for reference.

Appendix B

Effects of Initial Aspherical Seeds

In the main text, we have described how we added density perturbations as a source of initial asphericity for enhancing the later development of aspherical motion and instabilities. We used a somewhat arbitrary value of 1%. However, the actual density perturbations due to convection would certainly be different.

Here we examine how the initial density perturbation affect the energy deposition. We do not perturb the velocity fields because we find that the vector nature of the velocity makes it more difficult to construct a good profile. The profile should provide a good conservation of mass throughout the star, where density spans more than six orders of magnitude. In Figure B1 we plot the density and velocity for two models identical to Model 4 but with initial density perturbations smaller and larger by an order of magnitude. In both models, the behavior is very similar to that of Model 4. The similarity of the density profiles indicates that most of our results are insensitive to the details of the asphericity and density perturbations that would be present in a real star.

The velocity profiles of these models further indicate insensitivity to the initial density perturbations. Comparing

the profiles of two models at the same time slice, the differences are only 5%–10%. The similarity of the velocity profiles also ensures that our main results are robust against our choice of initial conditions.

For comparison, we also compute a model without any initial density perturbations, shown in Figure B2. Interestingly, this model shows a stiffer structure than our previous models, more akin to the one-dimensional models of Fuller (2017). The density inversion is slightly larger and with a steeper boundary, likely because the initial spherical symmetry results in Rayleigh–Taylor instabilities that take longer to grow and smooth it out. We also computed the Fourier asymmetry components A_n , and they are a few orders of magnitude lower than in our models presented in the main text. The velocity profiles in the right panel of Figure B2 are very similar to the models with density perturbations. We conclude that density perturbations should be added to capture the realistic growth of Rayleigh–Taylor instabilities, but that the magnitude of the perturbations does not strongly affect our results. Furthermore, we remark that in this simulation the spherical symmetry is strictly preserved so that the polar velocity field remains zero throughout the simulation. This ensures that the simulation is equivalent to its one-dimensional counterpart in that the

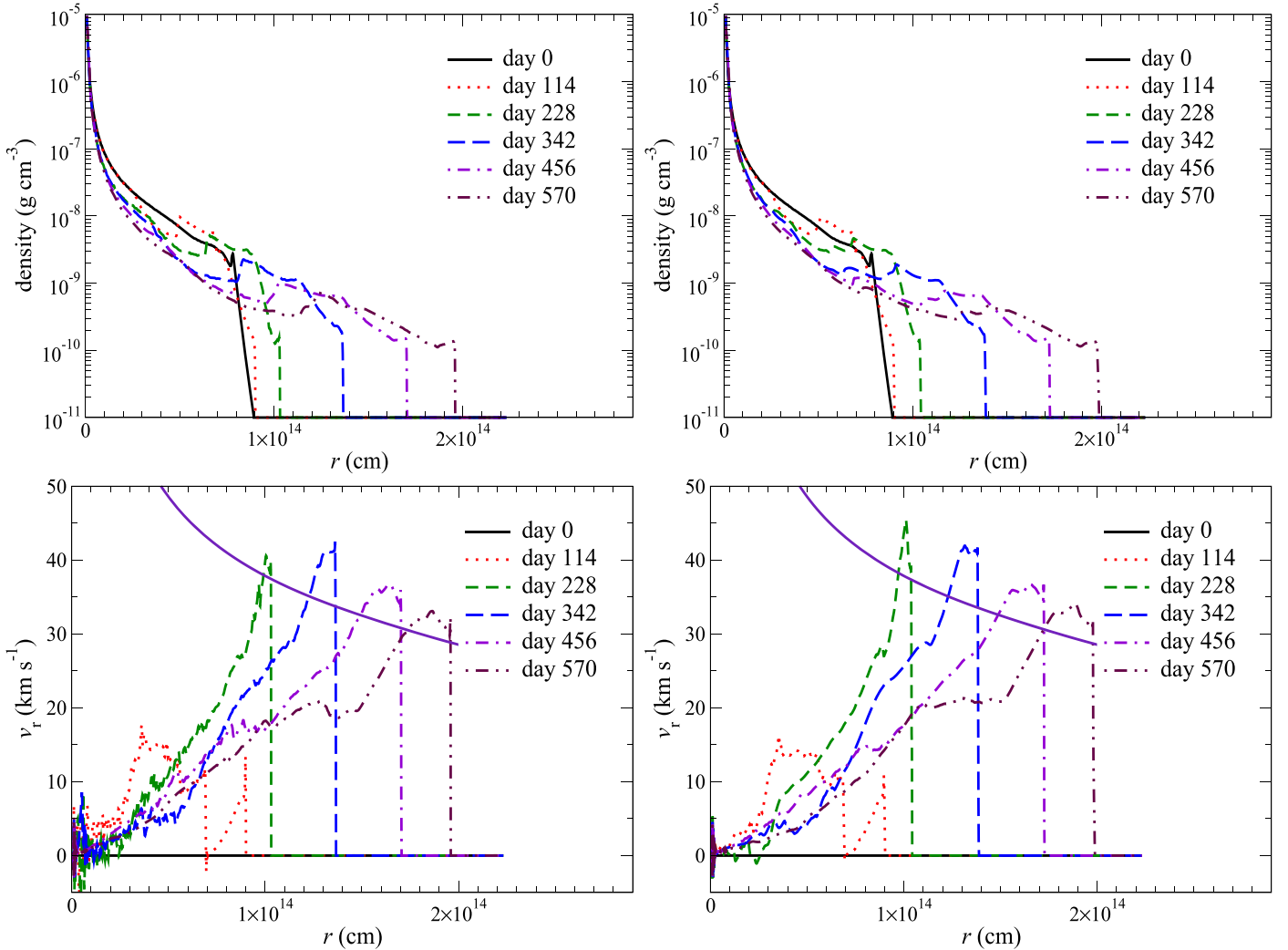


Figure B1. Top left: the angle-averaged density profiles of the test model based on Model 4 but with an initial asphericity seed of magnitude $\sim 0.1\%$. Top right: same as top left panel but for the model with an initial asphericity seed of magnitude $\sim 10\%$. Bottom panels: same as corresponding top panels but for the radial velocity profiles.

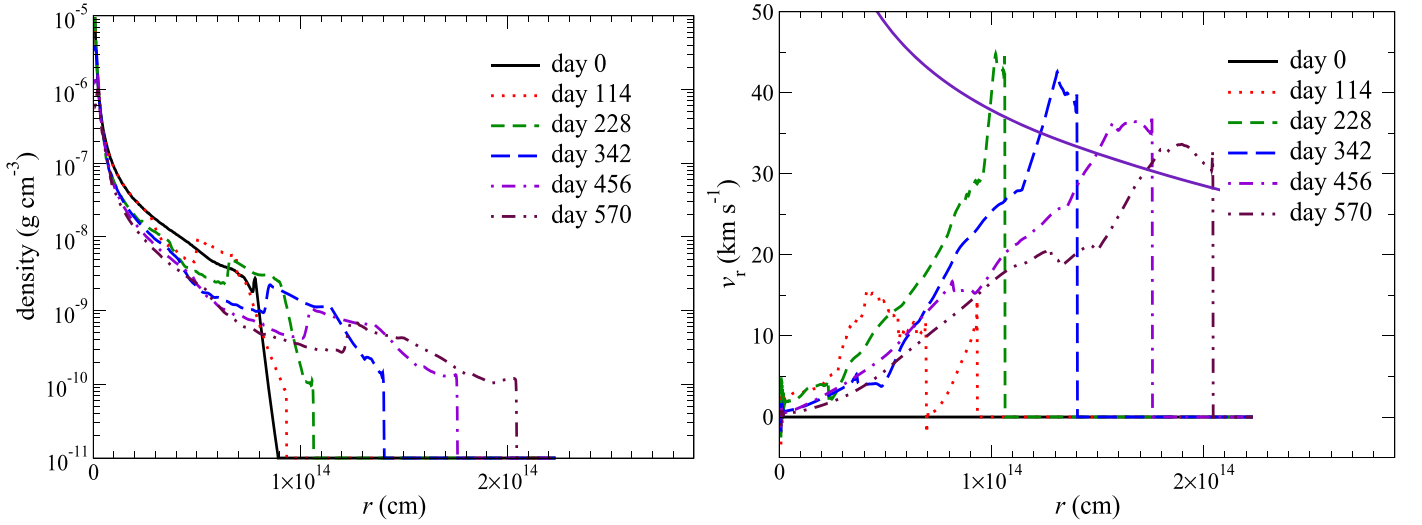


Figure B2. Left: the angle-averaged density profiles of Model 4s, which is identical to Model 4 but without density perturbations added to the initial conditions. Right: same as the left panel but for the velocity profiles.

pressure at a slice of constant radius is always balanced such that no spurious polar flow can be triggered when the model starts with spherical symmetry.

Appendix C

Effects of Smoothing Energy Deposition over Mass

Here we compare how the choice of smoothing the energy deposition over mass affects our results. When we calculate how the waves deposit the energy, we always smear the full energy deposition into a mass M_{dep} because in extreme cases the deposition sphere can recede toward the inner boundary. This poses a challenging modeling scenario because the sharp drop in the profile of density and sound speed can cause all the energy to be deposited in a single grid cell, such that the energy deposition is not well resolved. In fact, for the case of higher L_{dep} ($10^7 L_{\odot}$), the deposition length scale can become much

smaller than a grid cell, so it is numerically impossible to resolve the exact distribution of energy. To alleviate the problem, we define M_{dep} such that the energy deposition is always smeared into a few grid cells, such that our results are less sensitive to resolution.

To test the effect of this parameter on our results, we analyse two extra models, Model 4c and Model 4d, which have $M_{\text{dep}} = 0.05$ and $0.2 M_{\odot}$ respectively. In Figure C1, we plot the density and velocity profiles for the two models. Despite the fact that M_{dep} differs by a factor of four between the two models, we can see that there are almost no observable differences, except for minor changes in the peak velocity and the details of the density gradient. This provides evidence that the smearing procedure provides a good enough description of the energy deposition process in a resolvable manner.

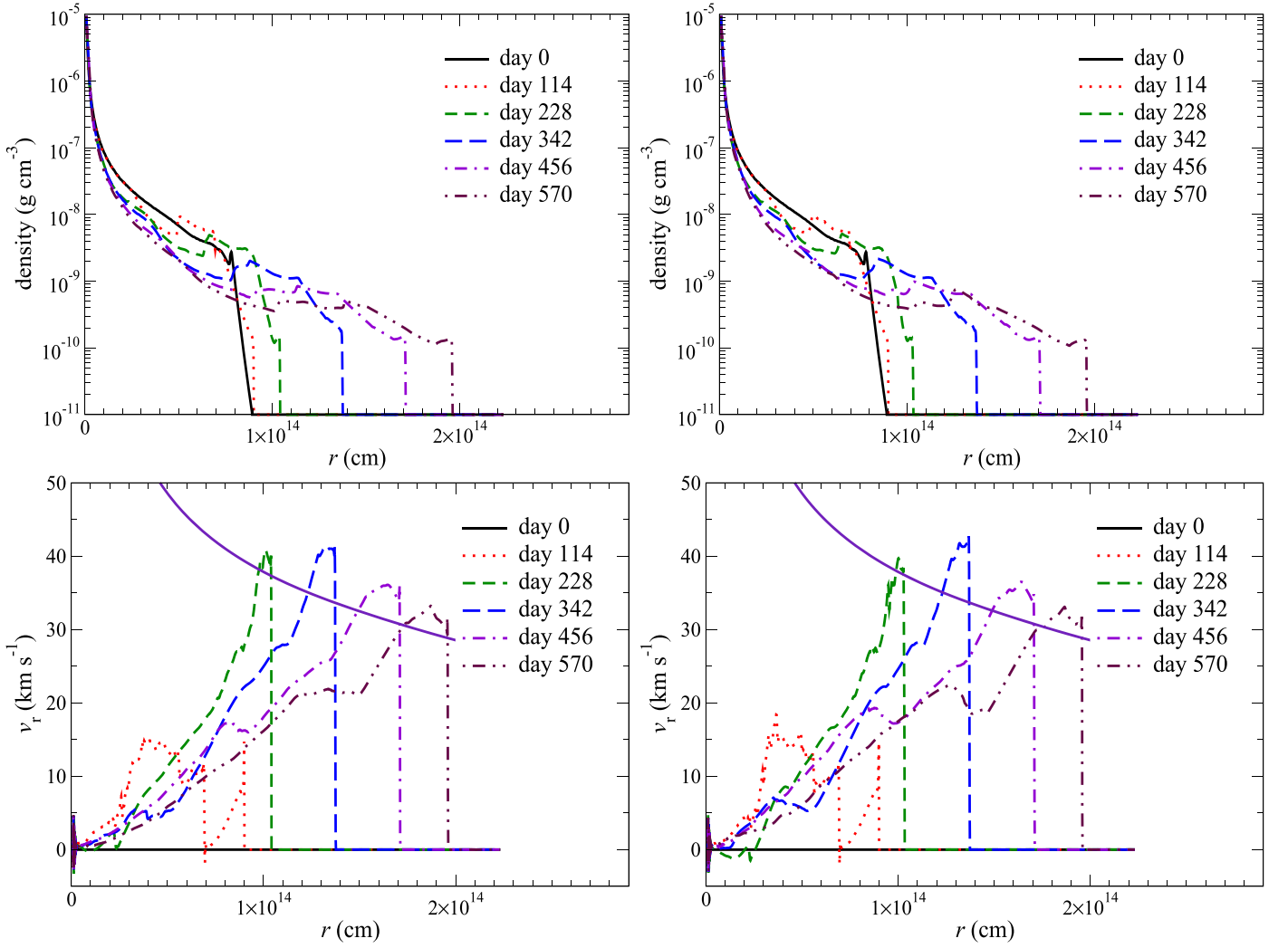


Figure C1. Top left: the angle-averaged density profiles of Model 4c, with M_{dep} (the mass over which energy deposition is smoothed) reduced to $0.05 M_{\odot}$. Top right: same as top left panel but for Model 4d with the M_{dep} increased to $0.2 M_{\odot}$. Bottom panels: same as corresponding top panels but for the radial velocity profiles.

Appendix D

Global Comparison of Test Models

Next, we compare the global energetics and the ejecta mass for the test cases examined in this appendix. They serve as a general diagnostic as to how sensitive each controllable parameter is to our final result. In Figure D1, we plot the total energy and its components for the test models, including Model 4 as a reference. We also plot the ejecta mass as a function of time. We can see that the choice of M_{dep} or aspherical seed size does not significantly change the energetics of the star. Model

4s shows a slightly larger expansion as described above, thus it has a slightly higher potential energy due to more energy inflow from the atmosphere.

With regard to the ejecta mass, Figure D1 shows that all the models are qualitatively the same, suggesting that the ejecta mass is not sensitive to the parameters presented above. All models show their peak at day 120 at $\sim 1.1 M_{\odot}$, and then the unbound mass gradually decreases until day 400 at $0.1\text{--}0.4 M_{\odot}$. At that point the models begin to deviate somewhat, but the final ejecta mass is always in the range $0.1\text{--}0.3 M_{\odot}$.

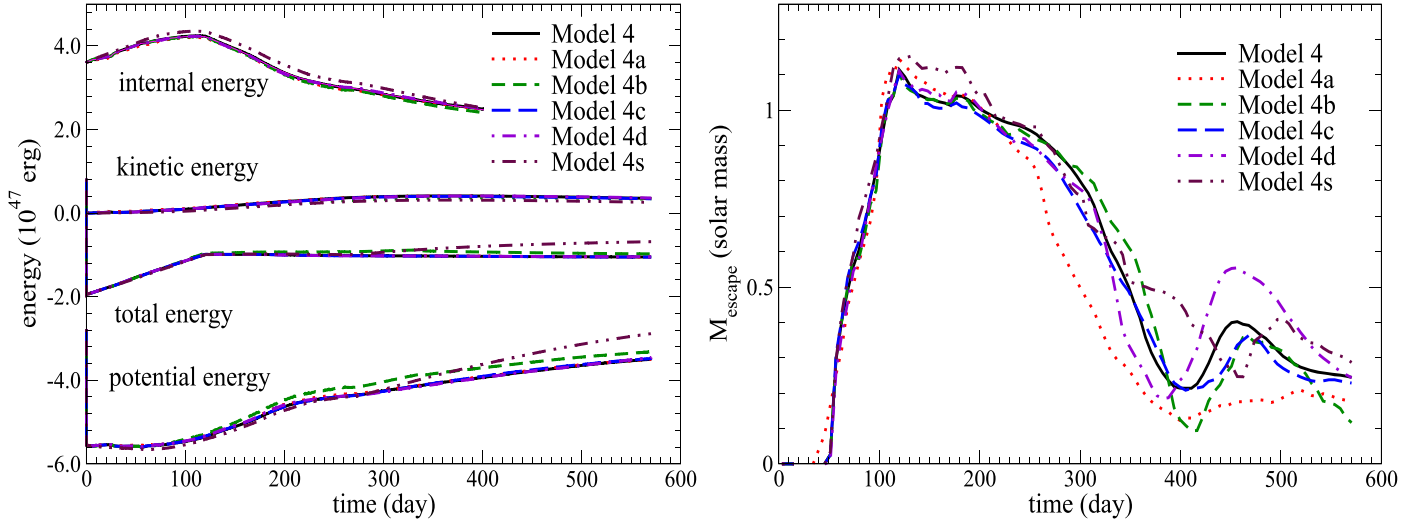


Figure D1. Left: the total energy, kinetic, gravitational, and internal energies of Models 4, 4a, 4b, 4c, 4d, and 4s. Right: same as left panel but for the ejecta mass.

Appendix E Notes on the Geometry

Our wedge simulations can be considered to be pieces of the star's equatorial or meridional plane. We use periodic boundary conditions in θ so that matter leaving one θ boundary enters the other θ boundary. For the computations of mass and energy, we define the volume elements $\text{vol}(r, \theta) = 8r^2 dr d\theta$ for a quadrant, automatically giving the volume of a sphere when integrated over both r and θ . In this choice, the 2D grid cells are intersections of 3D volume elements with the orbital plane, with each 3D volume element wrapping from the positive z -axis to the negative z -axis at constant radius. In the literature, axisymmetric models in the meridional plane are more frequently used for two-dimensional simulations. In the absence of forces breaking rotational symmetry, our geometry is physically identical to the meridional plane. We choose this geometry over a meridional plane geometry (in which case the volume elements would be $4\pi r^2 dr \sin\theta d\theta$) to give equal weight to all latitudes θ . Additionally, we choose periodic

boundary conditions because a closed boundary in the polar direction can strongly suppress the polar flow in the simulation.

In the main text, we noted that the energy deposition may generate a substantial horizontal flow in the inner layers of the star. To examine the choice of boundary conditions on this flow, we recompute Model 4 with reflective angular boundary conditions, explicitly suppressing any flow across those boundaries. We show in Figure E1 the angular velocities in both cases. In the model with periodic boundaries, a high-velocity flow has developed and remains substantial from day 114. On the other hand, the model with reflective boundaries shows lower velocities near the inner boundary, but similar velocities everywhere else. While the heating may drive mean flows in the inner layers, the angular motion appears turbulent in the outer part of the domain. The two models indicate that the dynamics of the outer part of the star are insensitive to the boundary conditions, but the possibility of rotational flows in the inner part of the star should be examined in future work.

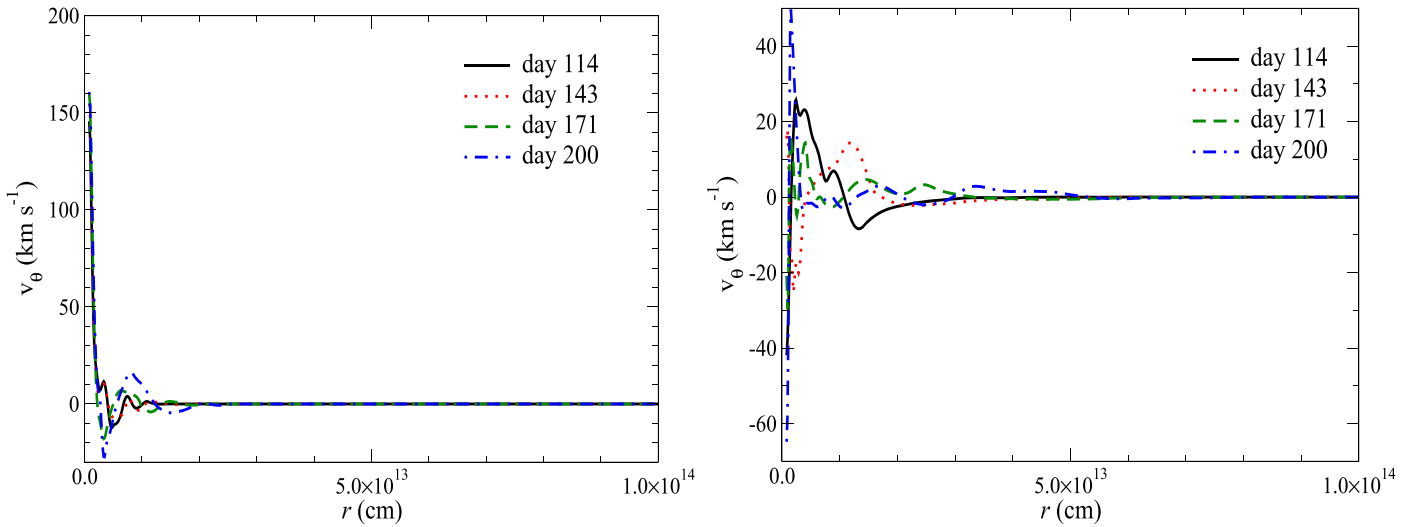


Figure E1. Left: the angular velocity of Model 4 at selected time frames. Right: same as left panel but for Model 4 with reflective angular boundaries.

ORCID iDs

Shing-Chi Leung <https://orcid.org/0000-0002-4972-3803>

Jim Fuller <https://orcid.org/0000-0002-4544-0750>

References

- Alvan, L., Strugarek, A., Brun, A. S., Mathis, S., & Garcia, R. A. 2015, *A&A*, **581**, A112
- Barth, T. J., & Deconinck, H. 1999, *Lecture Notes in Computational Science and Engineering 9: High-Order Methods for Computational Physics* (Berlin: Springer)
- Collins, C., Müller, B., & Heger, A. 2018, *MNRAS*, **473**, 1695
- Corsi, A., Ofek, E. O., Gal-Yam, A., et al. 2014, *ApJ*, **782**, 42
- Danieli, B., & Soker, N. 2019, *MNRAS*, **482**, 2277
- Duffell, P. C. 2016, *ApJ*, **821**, 76
- Elias-Rosa, N., Pastorello, A., Benetti, S., et al. 2016, *MNRAS*, **463**, 3894
- Fuller, J. 2017, *MNRAS*, **470**, 1642
- Fuller, J., Cantiello, M., Stello, D., Garcia, R. A., & Bildsten, L. 2015, *Sci*, **350**, 423
- Fuller, J., & Ro, S. 2018, *MNRAS*, **476**, 1853
- Gal-Yam, A., Arcavi, I., Ofek, E. O., et al. 2014, *Natur*, **509**, 471
- Goldreich, P., & Kumar, P. 1990, *ApJ*, **363**, 694
- Gräfener, G., & Vink, J. S. 2016, *MNRAS*, **455**, 112
- Groh, J. H. 2014, *A&A*, **572**, L11
- Ho, A. Y. Q., Goldstein, D. A., Schulze, S., et al. 2019, *ApJ*, **887**, 169
- Johnson, S. A., Kochanek, C. S., & Adams, S. M. 2018, *MNRAS*, **480**, 1696
- Khazov, D., Yaron, O., Gal-Yam, A., et al. 2016, *ApJ*, **818**, 3
- Kochanek, C. S., Fraser, M., Adams, S. M., et al. 2017, *MNRAS*, **467**, 3347
- Landau, L. D., & Lifshitz, E. M. 1959, *Fluid Mechanics* (Oxford: Pergamon Press)
- Leung, S.-C., Chu, M.-C., & Lin, L.-M. 2015, *MNRAS*, **454**, 1238
- Leung, S.-C., & Nomoto, K. 2017, in *Proc. NIC2016 14, Nucleosynthesis of Iron-Peak Elements in Type-Ia Supernovae* (Tokyo: JPS), 020506
- Leung, S.-C., & Nomoto, K. 2018, *ApJ*, **861**, 143
- Leung, S.-C., & Nomoto, K. 2019, *PASA*, **36**, e006
- Leung, S.-C., & Nomoto, K. 2020, *ApJ*, **888**, 80
- Leung, S.-C., Nomoto, K., & Blinnikov, S. 2019a, *ApJ*, **887**, 72
- Leung, S.-C., Nomoto, K., & Suzuki, T. 2020, *ApJ*, **889**, 34
- Leung, S.-C., Zha, S., Chu, M.-C., Lin, L.-M., & Nomoto, K. 2019b, *ApJ*, **884**, 9
- Mauerhan, J. C., Smith, N., Filippenko, A. V., et al. 2013, *MNRAS*, **430**, 1801
- McIey, L., & Soker, N. 2014, *MNRAS*, **445**, 2492
- Meakin, C. A., & Arnett, D. 2006, *ApJL*, **637**, L53
- Mihalas, D., & Mihalas, B. W. 1984, *Foundations of Radiation Hydrodynamics* (New York: Oxford University Press), 731
- Moriya, T. J., Förster, F., Yoon, S.-C., Gräfener, G., & Blinnikov, S. I. 2018, *MNRAS*, **476**, 2840
- Moriya, T. J., Yoon, S.-C., Gräfener, G., & Blinnikov, S. I. 2017, *MNRAS*, **469**, L108
- Morozova, V., Piro, A. L., Fuller, J., & Van Dyk, S. D. 2020, *ApJL*, **891**, L32
- Morozova, V., Piro, A. L., & Valenti, S. 2017, *ApJ*, **838**, 28
- Morozova, V., Piro, A. L., & Valenti, S. 2018, *ApJ*, **858**, 15
- Ofek, E. O., Cenko, S. B., Shaviv, N. J., et al. 2016, *ApJ*, **824**, 6
- Ofek, E. O., Sullivan, M., Cenko, S. B., et al. 2013, *Natur*, **494**, 65
- Ofek, E. O., Sullivan, M., Shaviv, N. J., et al. 2014, *ApJ*, **789**, 104
- Ouchi, R., & Maeda, K. 2019, *ApJ*, **877**, 92
- Pastorello, A., Smartt, S. J., Mattila, S., et al. 2007, *Natur*, **447**, 829
- Paxton, B., Bildsten, L., Dotter, A., et al. 2011, *ApJS*, **192**, 3
- Paxton, B., Cantiello, M., Arras, P., et al. 2013, *ApJS*, **208**, 4
- Paxton, B., Marchant, P., Schwab, J., et al. 2015, *ApJS*, **220**, 15
- Paxton, B., Schwab, J., Bauer, E. V., et al. 2017, *ApJS*, **234**, 34
- Paxton, B., Smolec, R., Schwab, J., et al. 2019, *ApJS*, **243**, 10
- Quataert, E., & Shiode, J. 2012, *MNRAS*, **423**, L92
- Ro, S., & Matzner, C. D. 2017, *ApJ*, **841**, 9
- Shiode, J. H., & Quataert, E. 2014, *ApJ*, **780**, 96
- Shivvers, I., Zheng, W., Van Dyk, S. D., et al. 2017, *MNRAS*, **471**, 4381
- Shivvers, I., Zheng, W. K., Mauerhan, J., et al. 2016, *MNRAS*, **461**, 3057
- Soker, N., & Gilkis, A. 2017, *MNRAS*, **464**, 3249
- Sorokina, E., Blinnikov, S., Nomoto, K., Quimby, R., & Tolstov, A. 2016, *ApJ*, **829**, 17
- Takata, M. 2016, *PASJ*, **68**, 91
- Timmes, F. X., Hoofman, R. D., & Woosley, S. E. 2000, *ApJS*, **129**, 377
- Tolstov, A., Nomoto, K., Blinnikov, S., et al. 2017, *ApJ*, **835**, 266
- Ulmschneider, P. 1970, *SoPh*, **12**, 403
- Wang, R., & Spiteri, R. J. 2007, *SJNA*, **45**, 1871
- Woosley, S. E. 2018, *ApJ*, **863**, 105
- Woosley, S. E., Blinnikov, S., & Heger, A. 2007, *Natur*, **450**, 390
- Woosley, S. E., Heger, A., & Weaver, T. A. 2002, *RvMP*, **74**, 1015
- Yadav, N., Müller, B., Janka, H. T., Melson, T., & Heger, A. 2020, *ApJ*, **890**, 94
- Yaron, O., Perley, D. A., Gal-Yam, A., et al. 2017, *NatPh*, **13**, 510
- Yoshida, T., Umeda, H., Maeda, K., & Ishii, T. 2016, *MNRAS*, **457**, 351
- Zha, S., Chu, M.-C., Leung, S.-C., & Lin, L.-M. 2019a, *ApJ*, **883**, 13
- Zha, S., Leung, S.-C., Suzuki, T., & Nomoto, K. 2019b, *ApJ*, **886**, 22